

CHALMERS



Synthetic Aperture Weather Radar

HIRAD GHAEMI

Department of Signals and Systems
Chalmers University of Technology
Göteborg, Sweden, 2008

EX062/2008



**Deutsches Zentrum
für Luft- und Raumfahrt e.V.**
in der Helmholtz-Gemeinschaft

SELEX
Sistemi Integrati
Gematronik Weather Radar Systems

SYNTHETIC APERTURE WEATHER RADAR

Student:

Hirad Ghaemi

Supervisors:

Prof. Dr. Mats Viberg¹
Michele Galletti²

Dr. Thomas Boerner²
Dr. Frank Gekat³

¹Signal and System Department, Chalmers University of Technology.

²Microwave and Radar Institute, DLR.

³SELEX-SI Gematronik Co.

Contents

I	Preamble	2
II	Acknowledgments	4
III	List of Symbols	6
1	Ground-based CSAR	9
1.1	Sectorial Phased Array	9
1.2	Azimuth Compression in Strip-map CSAR	19
1.3	Super-Resolution Strip-map CSAR	29
1.4	Concluding Remarks	36
2	Ground-based PSAR	39
2.1	Precipitation Imaging	39
2.1.1	Doppler Spectrum Estimation	41
2.1.2	Autofocusing (Motion Compensation, Phase Error Mitigation and Range Migration Correction)	51
2.2	Reflectivity and Rain Rate Estimation	65
2.3	Concluding Remarks	71
	Bibliography	72

Part I

Preamble

To enhance the along-track resolution in radar imaging, the synthetic aperture radar (SAR) technique has been widely used. It has been found a very robust tool in a broad variety of applications. One of the applications which might be of great interest is precipitation imaging and measurement with much higher resolution and more accurate parameter estimation than the conventional Doppler weather radar(s).

This thesis mainly focuses on implementation of the precipitation synthetic aperture radar technology (PSAR) for ground-based Doppler weather radars whereas both airborne-based and spaceborne-based PSAR have already been investigated.

A few algorithms, which are slightly different from each other, employed to do the SAR focusing on precipitation with and without clutters, will be stated in details. Prior to this chapter, an introductory chapter is dedicated to ground-based circular SAR (CSAR) for a point scatterer in terms of beamwidth/angular improvement of the radiation pattern.

Apart from the algorithms chosen to implement PSAR, several aspects and limitations of the ground-based PSAR versus its two counterparts will be discussed in details.

The goal in this report is to give the reader a clear idea about the capability of SAR technique in meteorological applications, specifically for ground-based weather radars, which has been in fact the major purpose of this work.

Part II
Acknowledgments

I would like to thank those individuals and organizations supporting me throughout this work.

The propagation and scattering group, at microwave and radar institute DLR Oberpfaffenhofen, has provided me with a decent environment. My boss, Dr. Thomas Boerner here in DLR, has fully supported me and helped me out of several bureaucratic issues which I had encountered especially at the beginning of my work.

I thank Dr. Frank Gekat, my employer at SELEX-SI Gematronik, Dr. Boerner, and Mr. Michele Galletti, my supervisors at DLR, who have given me this opportunity to work in DLR. Dr. Gekat and his colleague Mr. Peter Goelz have provided me with several series of data which I have used to test the algorithms.

I would like to thank my academic supervisor, Prof. Dr. Mats Viberg, at the department of signal and system, Chalmers University of Technology. I have received several useful ideas and suggestions from him throughout my project.

I am very grateful to Mr. Christian Andres and Mr. Jens Fischer, working at SAR group in DLR, who had helped me to understand a few important principles and some practical aspects in SAR.

Finally, I appreciate discussion as well as tips from my colleagues Dr. Andreas Danklmayer, Dr. Thomas Molkentin and Dr. Nicolas Marquart in DLR.

Part III
List of Symbols

ω_r	Angular velocity of rotating antenna
θ_a	Elevation angle of antenna
θ_H	Azimuthal half-power beamwidth of antenna
θ_V	Vertical half-power beamwidth of antenna
λ	Wavelength at carrier frequency in free space
ϕ_t	Azimuthal angle of target
θ_t	Elevation angle of target
ϕ	Angular position in azimuth plane
D	Distance from rotation center to antenna's phase center
rpm	rpm of the antenna
PRF	Pulse repetition frequency of radar in Hz
PRI	Pulse repetition interval of radar in sec
σ	Radar Cross section(RCS) of target or group of targets
δ_ϕ	Azimuth angular resolution
N	The number of azimuth samples within the integration time
c	The light velocity
f_c	Carrier frequency of radar
τ	Pulse width of transmitted pulse
B	Bandwidth of receiver
R_n	n^{th} range bin in meter
$f(R, \phi_t)$	Reflectivity function of the target scene
$w(R, \phi)$	SAR's prefilter
$h(R, \phi)$	SAR's postfilter
v	Samples of additive Gaussian noise
RS	Range sampling rate in meter
P_t	Transmitted power
P_{av}	Averaged received power
G_a	Antenna Gain
l_h	The maximum horizontal length of antenna
G_p	The processing gain in SAR
v_a	The Nyquist or unambiguous velocity
α	Complex amplitude of scatterer/distributed scatterers
Δ_a	Doppler spread of data samples along azimuth in Hz
f_a	Doppler center of data samples along azimuth in Hz
d_a	Delay/peak location of data samples along azimuth
Δ_r	Doppler spread of data samples along range in Hz
f_r	Doppler center of data samples along range in Hz
d_r	Delay/peak location of data samples along range

RSI	Range sampling interval in sec
θ_s	Synthetic beamwidth or SAR angular resolution
θ_r	The resultant pattern in SAR
V_r	Platform velocity
T_d	Decorrelation time
γ	Phase error or arg. of multiplicative noise along azimuth
χ	Phase error due to range migration
L_r	The total loss of transceiver, radar system
K_r	Propagation loss due to scatter and absorption in rain in dB/km
Z	Reflectivity factor of precipitation mm^6/m^3
R_r	Rain rate in mm/hr
σ_v	Doppler spectral width of distributed targets
P_{psar}	Processed power in PSAR

Chapter 1

Ground-based CSAR

1.1 Sectorial Phased Array

The geometry of the ground-based rotating antenna along with a stationary point scatterer above the ground is depicted in figure (1.1).

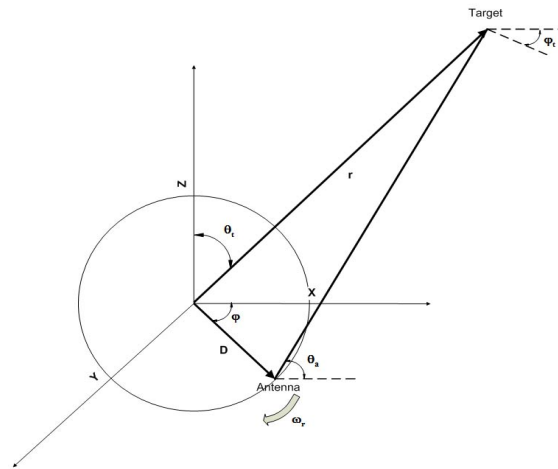


Figure 1.1: The geometry of ground-based CSAR

The antenna is rotating with a constant angular velocity. The relative motion/displacement between sensor and target provides the phase history carried by the received complex fields to be exploited in the SAR processor with the aim of creating a synthetic pattern with narrower beamwidth than that of real antenna. In other words the received samples contain different phases with respect to each other based on the time of reception which in fact associates with the corresponding relative position of antenna at that specific time. This phase history has the quadratic shape due to the process

of approaching and retreating from the target occurred by the regular motion of radar. In order to sum the received samples from the same target in a coherent way, what one should do is to multiply the consecutive samples by unit-amplitude samples (actually they are the unit-energy samples) having the relative phases opposite (conjugate) to those of received samples and then perform the summation.

Assuming the PRF is very high, by following the simple approach described for linear SAR in the presence of the stationary point target in the first chapter of Franceschetti and Lanari (1999) the output of the SAR matched filter, i.e., azimuth compression or equivalently the processed pattern in terms of angular position in azimuth, $F(\phi)$, can be shown to be:

$$F(\phi) = \sum_{n=-\infty}^{\infty} j^n \exp(j(\phi_2 - \phi_1 + \phi_t + \pi)n/2) \times J_n(\beta) \times \times \text{sinc}(n/2(\phi_2 - \phi_1)) \times \exp(j\frac{n\phi}{2}) \quad (1.1)$$

where

$$\begin{aligned} \phi_1 &= \max(\phi, \phi_t) - \frac{\theta_H}{2} & \phi_2 &= \min(\phi, \phi_t) + \frac{\theta_H}{2} & |\phi - \phi_t| &\leq \frac{\theta_H}{2} \\ \beta &= 4\pi/\lambda \cos(\theta_a) \sin(\theta_t) \sin(\phi - \phi_t) \end{aligned}$$

The above relations emphasize the simple fact that the target is situated within the half power beamwidth of the antenna which is illuminating and then processing the received complex returns from it. One may think of this CSAR scenario as a sectorial (partially circular) phased array (Balanis, 2005) of isotropic series of elements, antennas, trying to focus the beam towards a specific direction which is the position of the point target above the radar's platform or ground surface. To perceive the difference between this and its two counterparts i.e., linear array and circular array, these three scenarios with their corresponding array-factor patterns (Mailloux, 2005) are illustrated in figure (1.2). The plot at the last row in figure (1.2) corresponds to our case here. In figure (1.3) the desired scenario is projected on a plane to manifest how the process of target illumination from a single antenna moving on a circular path (a few consecutive positions of the radar or equivalently a few samples extracted in sequence by radar are marked by "x" in figure (1.3)), works. This mode of illumination is called stripmap mode in SAR technology. Thus, through an analogy performed by partially circular array antenna, after some mathematical manipulation with the aid of the classical

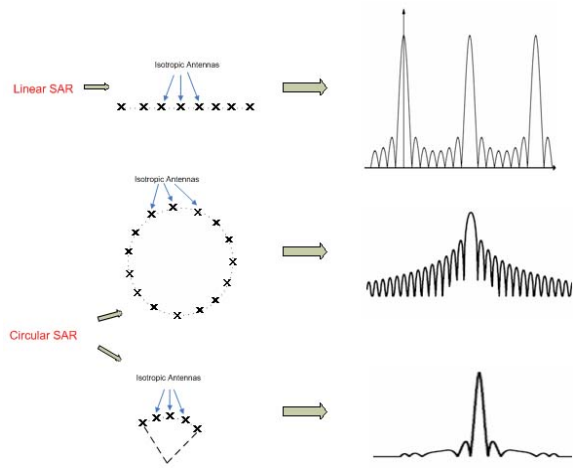


Figure 1.2: The three configurations of phased-array antennas

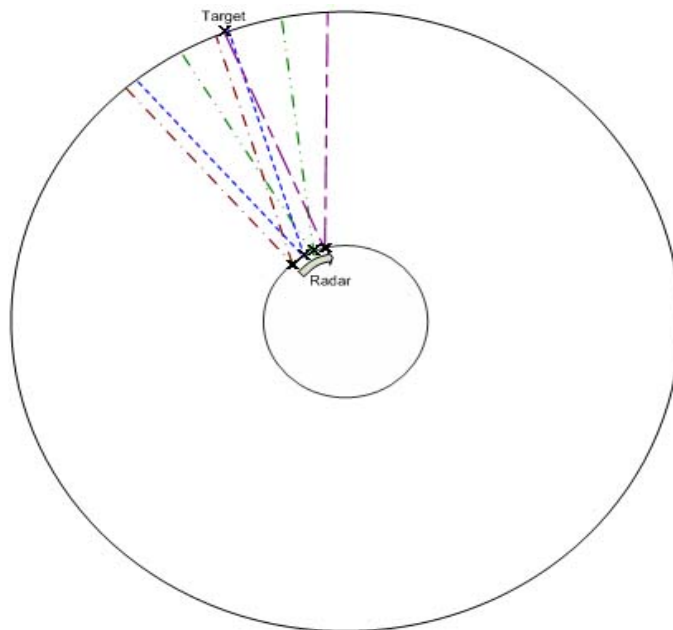


Figure 1.3: The point target-illumination process

approach explained in Balanis (2005) for both linear and circular phase array, the corresponding array factor for isotropic elements, $\mathbf{AF}(\phi)$, is:

$$\mathbf{AF}(\phi) = \sum_{n=-\infty}^{\infty} j^n \frac{\exp(jn\theta_H/2)}{\exp(jn\theta_H/(4N+2))} \times \exp(j(\phi_t + \pi)n/2) \times J_n(\beta) \times \frac{\sin(n\theta_H/2)}{\sin(n\theta_H/(4N+2))} \times \exp(j\frac{n\phi}{2}) \quad (1.2)$$

where

$$2N+1 = \frac{\theta_H}{\alpha} \quad |\phi - \phi_t| \leq \theta_H/2 \quad \alpha = \frac{\pi \times rpm}{30 \times PRF}$$

The equations (1.1) and (1.2) show the same radiation or processed pattern. In both cases the final resultant pattern is obtained by multiplication of processed pattern (the output matched filter, MF_{out}) and the real antenna pattern (denoted as HPBW in corresponding figures) which is not isotropic. Indeed, the resultant pattern determines the resolution in both identical interpretations.

As an example, separate patterns and the resultant pattern are plotted in figure (1.4) and figure (1.5) respectively (note that due to the symmetry, simply half of the entire patterns are drawn). In SAR, it is well known that the Fourier Transform (FT) of the data along azimuth gives the image of the target. For the point scatterer, its FT of the received phase-modulated (PM) complex signal along its azimuthal position is given as (based on Fresnel approximation for far field, i.e., conversion from PM signal to a chirp signal which is linearly frequency modulated (LFM) signal) :

$$S_c = A \cdot \text{sinc}\left(\frac{\theta_H}{2\omega_r}(\omega - \omega_t)\right) \quad (1.3)$$

where

$$\omega_t = \frac{4\pi}{\lambda} \cdot D \cdot \cos(\theta_a) \cdot \sin(\theta_t) \cdot \omega_r \cdot \phi_t \quad \omega_r = \frac{\pi}{30 \times rpm}$$

“A” is the magnitude of the target’s reflectivity factor.

In equation (1.3) another important assumption has been made, which is:

$$|\theta_t - \theta_H| \leq \frac{\theta_V}{2} \quad (1.4)$$

As anticipated, the center frequency, ω_t , which is commonly called Doppler frequency center, is linearly proportional to the angular position of the target,

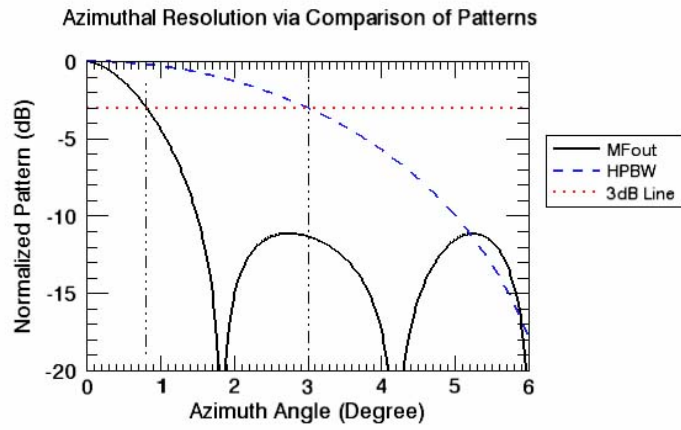


Figure 1.4: The real antenna(HPBW) and processed(MFout) patterns for $\theta_H = 6^\circ$, $f_c = 10GHz$, $D = 1.7m$, $PRF = 200Hz$, $rpm = 0.5$, $\theta_a = 10^\circ$

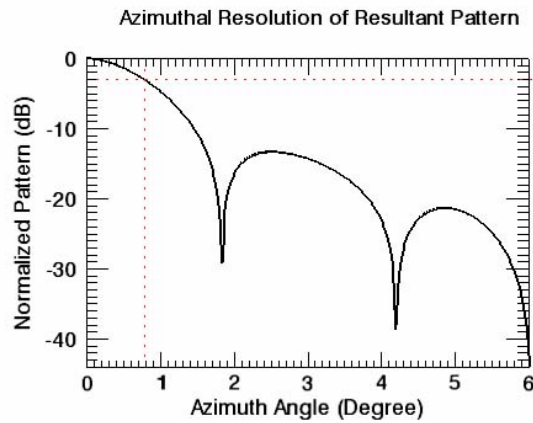


Figure 1.5: The resultant pattern that is the multiplication of MFout(black solid curve) pattern and HPBW (blue dashed line) pattern plotted in figure(1.4)

i.e., ϕ_t .

Accordingly the angular resolution of the azimuth is given as:

$$\delta_\phi \approx \frac{\lambda}{2D \cdot \cos(\theta_a) \cdot \sin(\theta_t) \cdot \theta_H} \quad (1.5)$$

Since the target is not visible by radar in the continuous manner, to achieve the aforementioned resolution the PRF, pulse repetition frequency of the transmitted rectangular pulse which is also the sampling rate along azimuth, must be high enough to provide one sample per minimum angular/spatial resolution. In other words it is essential that the sampling rate or PRF satisfies the following criterion similar to the one stated in Franceschetti and Lanari (1999) for linear SAR.

$$PRF \geq \frac{\omega_r}{\delta_\phi}$$

Therefore the maximum integration time, IT_m , that is the maximum possible coherent time during which the target remains coherent within the maximum illumination interval, is

$$IT_m = \frac{\theta_H}{\omega_r} \quad (1.6)$$

While radar is illuminating a target there is a possibility that the resultant/processed pattern has more than one mainlobe (the additional lobes are called grating lobes). To avoid such grating lobes which cause ambiguity in azimuth, it's necessary for the radar to have a minimum lower bound on PRF. To obtain this lower bound, first the discrete form of processed pattern is calculated. The corresponding pattern, i.e., $F(\phi_n)$, irrespective of antenna's radiation pattern, is as follows (Franceschetti and Lanari, 1999):

$$F(\phi_n) = \frac{\sin(2\pi/\lambda \cdot D \cdot \cos(\theta_a) \cdot \sin(\theta_t) \cdot \Delta\phi^2 \cdot n(2N + 1 - n))}{\sin(2\pi/\lambda \cdot D \cdot \cos(\theta_a) \cdot \sin(\theta_t) \cdot \Delta\phi^2 \cdot n)} \quad (1.7)$$

where

$$\phi_n = n \cdot \Delta\phi \quad \Delta\phi = \alpha \quad 2N + 1 = \frac{\theta_H}{\Delta\phi} \quad |n| \leq N$$

Therefore the minimum PRF to avoid the grating lobes is:

$$PRF_{min} = \frac{\pi \cdot rpm \cdot \theta_H \cdot D \cdot \cos(\theta_a) \sin(\theta_t)}{15 \cdot \lambda} \quad (1.8)$$

To see how a wrong choice of PRF can create one or more extra lobes or equivalently grating lobe(s), an example is demonstrated for both individual

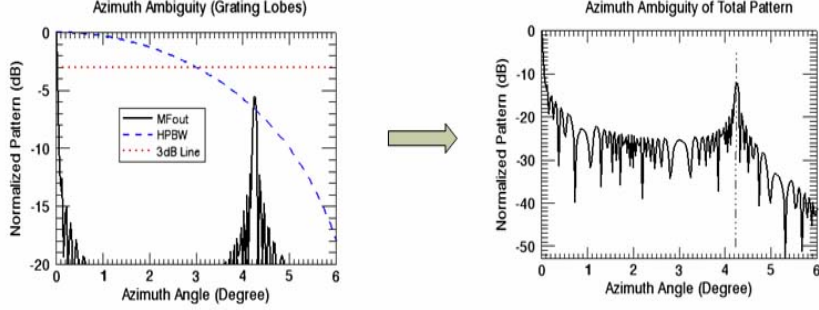


Figure 1.6: The grating-lobe phenomenon due to a low PRF for $\theta_H = 6^\circ$, $f_c = 10GHz$, $D = 102m$, $PRF = 100Hz$, $rpm = 0.5$, $\theta_a = 10^\circ$

patters(on the left side) and total pattern(on the right side) as well in figure(1.6). On the other hand the upper bound for PRF is determined by maximum unambiguous range as well as hardware limitation in maximum speed of sampling(herein the latter is ignored).

To circumvent ambiguity in range estimation for the maximum unambiguous ground range, GR_{max} , the upper bound of PRF is given as

$$PRF \leq \frac{c}{2\theta_V \cdot GR_{max} \cdot \tan(\theta_a) \cdot \sec(\theta_a)} \quad (1.9)$$

Now, at this step, it's worth investigating the amount of influence of six key parameters, i.e., θ_H , f_c , D , PRF , rpm , θ_a , on resolution regarding imaging of a point scatterer. The following six images demonstrate their impacts for a rotating ground-based radar with flexible parameters with initial values, $\theta_H = 1^\circ$, $f_c = 5GHz$, $D = 1.6m$, $PRF = 200Hz$, $rpm = 0.5$, $\theta_a = 40^\circ$. Figure(1.7) shows the change of resolution as a result of two antennas with two different HPBW.

As expected in any SAR systems, the smaller the antenna the higher the resolution. This parameter is one of the most significant one.

The other influential parameter, specifically in ground-based circular SAR which distinguishes that from linear SAR, is the radius of platform, D . Figure (1.8) points out this fact.

It is easy to notice that the larger D , the much better the resolution.

According to figure (1.9) the increase in carrier frequency is also improves the azimuthal resolution up to some extent.

Figure (1.10) and figure(1.11) illustrate the impact of PRF and angular ve-

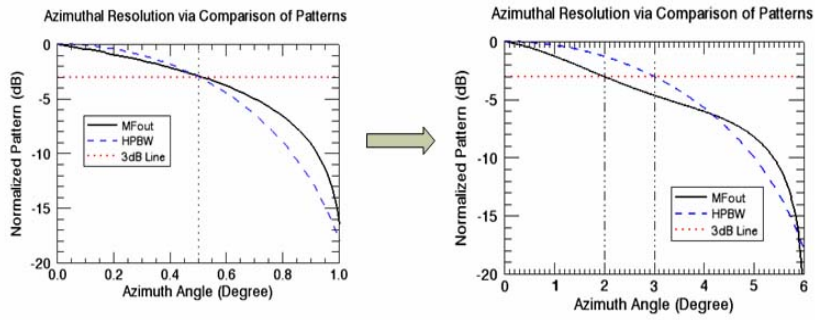


Figure 1.7: The effect of antenna size in achieving the angular resolution in azimuth for processed pattern, from $\theta_H = 1^\circ$, on the left, to $\theta_H = 6^\circ$, on the right.

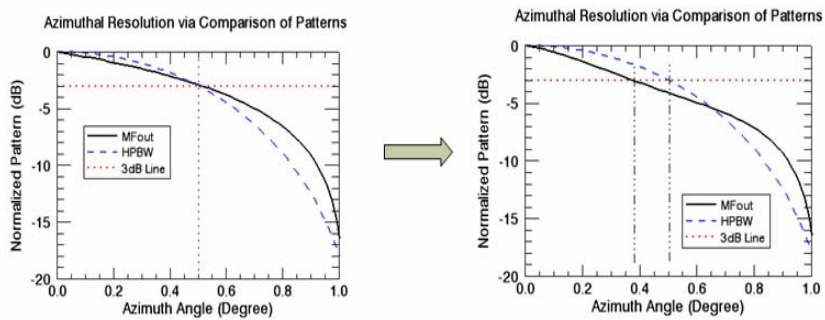


Figure 1.8: The effect of D in achieving the angular resolution in azimuth for processed pattern, from $D = 1.6m$, on the left, to $D = 48m$, on the right.

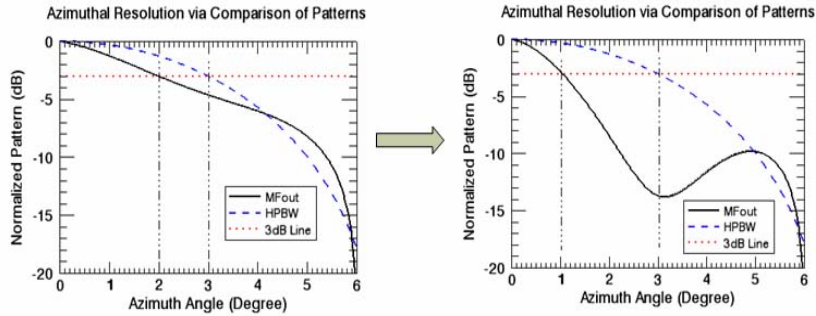


Figure 1.9: The effect of carrier frequency in the angular resolution along azimuth for processed pattern, from $f_c = 5GHz$, on the left , to $f_c = 10GHz$, on the right.

locity on resolution, respectively. Despite the increase in SNR due to increase in ratio PRF/rpm within the integration interval, neither of them cause any change in resolution. However; it will be shown in the next chapter that the reverse is true.

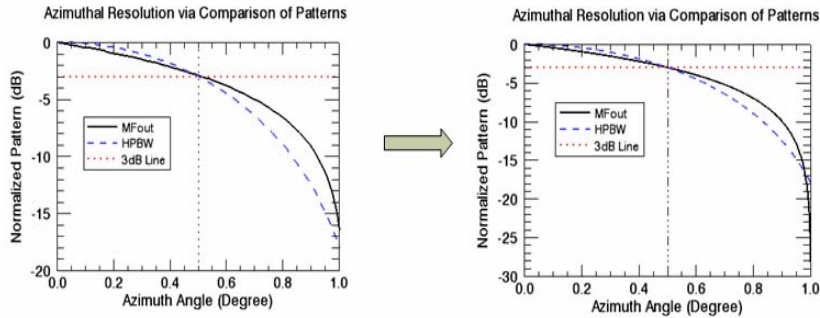


Figure 1.10: The effect of PRF in the angular resolution along azimuth for processed pattern, from $PRF = 200Hz$, on the left , to $PRF = 2000Hz$, on the right.

The last parameter of less significance is the elevation angle of antenna. This basically has no considerable impact on resolution as depicted in figure (1.12). Note that the elevation angle of the target must have a value close to that

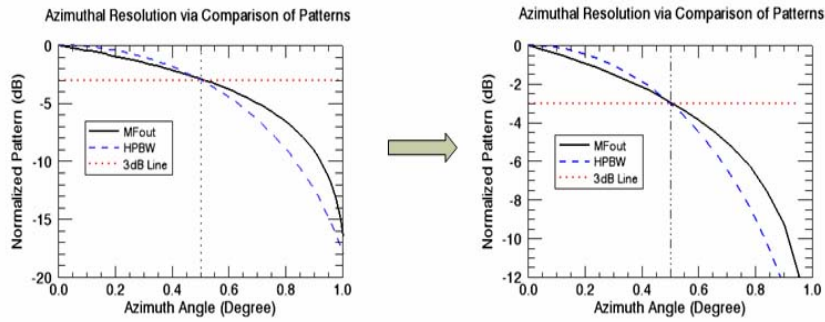


Figure 1.11: The effect of antenna's angular velocity, rpm, in the angular resolution along azimuth for processed pattern, from $rpm = 0.5$, on the left , to $rpm = 6$, on the right.

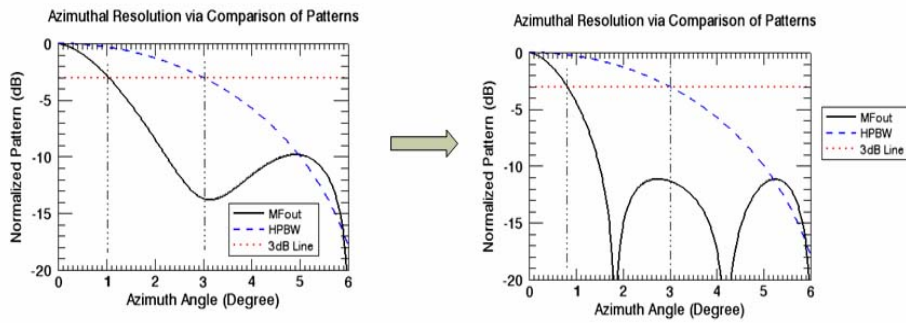


Figure 1.12: The effect of antenna's elevation angle in the angular resolution along azimuth for processed pattern, from $\theta_a = 40^\circ$, on the left , to $\theta_a = 10^\circ$, on the right.

of antenna within its vertical HPBW.

In short, enhancement in the resolution accompanies with several influences on the processed pattern including, the decrease in the width of mainlobe plus the distance between the first sidelobe and the maximum peak and even increase in the sidelobe level.

1.2 Azimuth Compression in Strip-map CSAR

Since the Doppler radar whose data are used in this project, is a simple pulse radar, which means that the transmitted signal is narrowband unlike many SAR systems with frequency modulation such as LFM in order to increase the range resolution, herein the range resolution is restricted by pulse width. Furthermore; the corresponding bandwidth of the receiver is designed to be almost matched to the transmitted pulse, i.e., $B\tau \approx 1$. Thus, in this project, all attempts are to compress and focus the received samples along azimuth at each range bin. In other words, the reconstruction algorithm of SAR is basically considered to be one dimensional rather than two.

Following a simple procedure (Brown, 1967; Broquetas et al., 1997) for geometry demonstrated in figure(2.1), the complex received signal, $S(R_n, \phi)$, at a specific range bin, R_n , is obtained

$$S(R_n, \phi) = \int_{\phi_t} A(R_n, \phi - \phi_t) f(R_n, \phi_t) \exp(-j \frac{4\pi r(R_n, \phi - \phi_t)}{\lambda}) d\phi_t + v \quad (1.10)$$

in which

$$\begin{aligned} r(R, \phi) &= \sqrt{R^2 + 2D (D + R \cos(\theta_a)) (1 - \cos(\phi))} \\ &\approx R + D (1 - \cos(\phi)) (\frac{D}{R} + \cos(\theta_a)) \end{aligned} \quad (1.11)$$

Here the weighting function “A” is antenna radiation pattern, two-way power pattern within half power beamwidth, in the antenna’s far field. The log constant of radar is ignored here as it has no effect on the SAR compression process.

Suppose the SAR’s prefilter (Brown, 1967) (the filter defines the interaction between reflectivity function of target and the radiating antenna within the illumination time) is

$$w(R_n, \phi) = A(R_n, \phi) \exp(-j \frac{4\pi r(R_n, \phi)}{\lambda}) \quad (1.12)$$

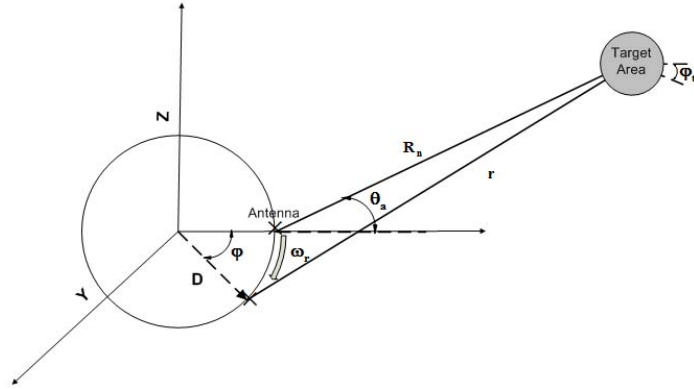


Figure 1.13: The geometry of CSAR

Taking a closer attention to equation (1.10), one can easily deduce the following convolution for the received signal

$$S = w * f + v \quad (1.13)$$

“*” stands for convolution. The additive Gaussian noise (which is dominantly the thermal noise at receiver) can be neglected in the following process as long as the SNR of desired target(s) is high enough. Moreover; the multiplicative phase noise is disregarded here for the sake of simplicity based on the fact that the scene is unperturbed which is proven to be wrong for precipitation in the next chapter. Thus the reflectivity factor is not contaminated by the phase error(Brown, 1988) causing the random fade (Raney, 1980) and also the target field is assumed to be almost static/quasi-static (not a random field). However; these couple of last assumptions are removed in the next chapter regarding precipitation imaging.

As a result, the matched filter, also called SAR postfilter, “h”, should have the following form to retrieve the target reflectivity function

$$h(R_n, \phi) = \gamma(\phi) \bar{w}(R_n, -\phi) \quad (1.14)$$

Where γ is a weighting function along azimuth. Also in this thesis the complex conjugate is shown by “bar” sign.

To avoid high-level side lobes caused by azimuth compression, instead of constant amplitude(rectangular tapering) the weighting function may have Gaussian shape which is the favorite choice in many SAR’s application. Here both the Hamming window (with SLL about -42dB) and Chebyshev tapering with variable SLL below -40dB are employed as amplitude weighting function. The corresponding results are almost the same for SLL equal to -40.

To see how the above simple CSAR algorithm works, hereby a couple of examples are taken into account.

In the first example, the ground-based Doppler weather radar has a big reflector antenna with parameters as stated in table(1.1). Figure(1.14) shows the structure of the rotating reflector and its corresponding fixed pedestal.

Table 1.1: Parameters of Radar and its Reflector Antenna

Parameters	Values
θ_H	1°
θ_V	1°
τ	0.5us
P_t	250 KW
G_a	45 dB
λ	0.053 m
PRF	1200 Hz
rpm	6 rpm
D	1.7 m
θ_a	0.4°
RS	50 m
Polarization	H

Since the distance D is very small compared to the size of antenna, the desired phase history imposed by SAR's prefilter has a very small changes which means that the processed pattern is much wider than the real antenna pattern and as a consequence the resultant pattern has the same resolution as that of antenna.

Raw and focused image for an area consisting of strong clutters, with the aim of clutter focusing, are illustrated in figure(1-15). As expected the resolution has not changed.

To measure the enhancement of resolution, slow-time domain samples of a strong ground clutter for both raw and processed data are plotted in figure (1-16).

In the second experiment, the antenna is a small standard horn whose parameters are listed in table(1.2). Those unmentioned ones are the same as that of the reflector.

According to figure(1-17) unlike the former case, because of quite large distance D with respect to size of antenna, i.e., large D and large antenna's beamwidth, the achieved resolution is very impressive and indeed, it is in the order of reflector's resolution, therefore it's comparable. Again, in order to recognize the amount of resolution improvement, the width of the pattern of

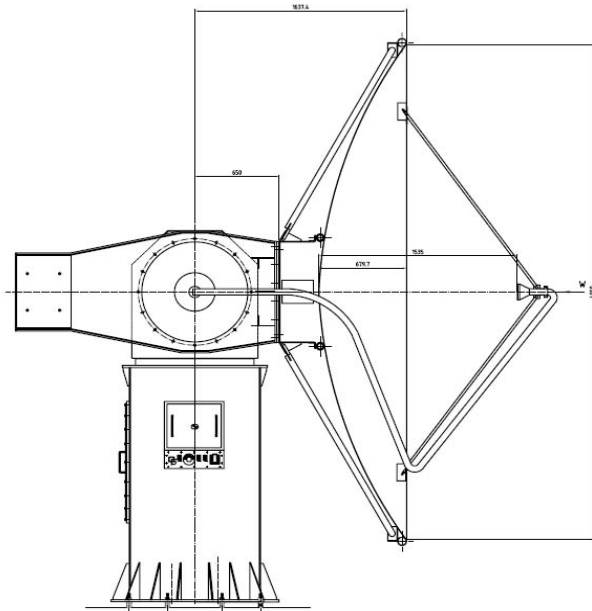


Figure 1.14: The reflector and its platform structure

Table 1.2: Parameters of standrad horn

Parameters	Values
θ_H	26.2°
θ_V	23.7°
G_a	17.5 dB
D	≈ 4 m
Polarization	V

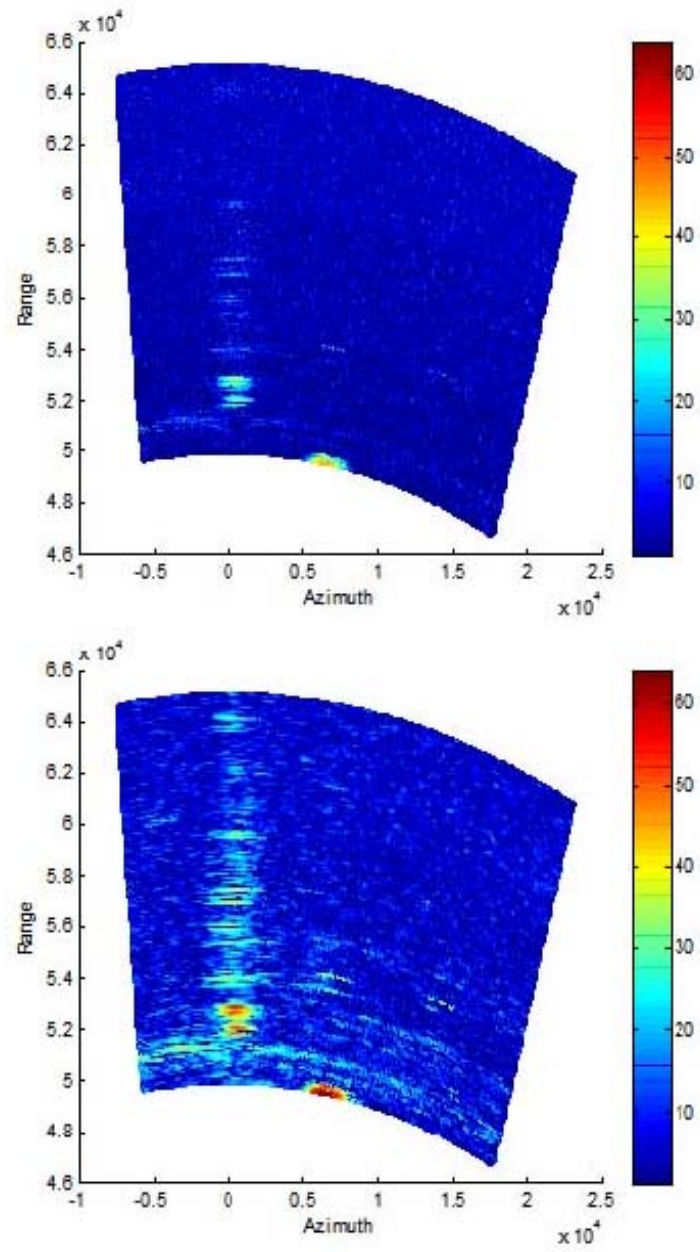


Figure 1.15: Raw (at top) and focused (at bottom) images using the reflector antenna

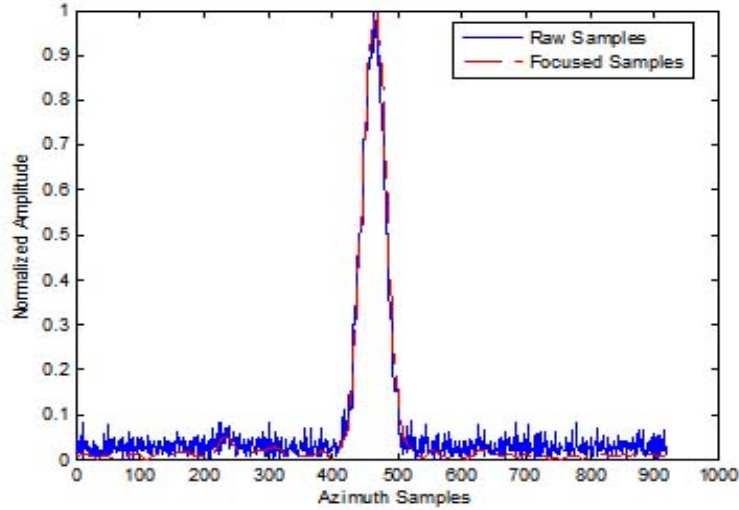


Figure 1.16: Raw and focused azimuth samples at a specific range from reflector

time-domain samples before and after SAR's postfilter are to be compared, as shown in figure (1.18). The angular resolution is changed from 26.2° to about 1.5° .

Note that, to both cases above, the full-synthetic aperture, which is about the HPBW of antenna, has been applied.

It's noticeable that there are some areas which look still partly focused in figure (1-17). It occurs due to the uncompensated motion from that target moving and therefore some part of them are filtered out by the SAR's postfilter which is in fact, a LPF. To cope with this defocusing, the complex postfilter must be shifted in frequency domain which means conversion from LPF to BPF to allow the most part of the signal's energy to pass through. This can be done adaptively by multiplying another phase term to the aforementioned postfilter. Either through calculation of the amount of increase in SNR in an iterative manner or alternatively, checking the image quality visually, one can readily determine the additional phase term along azimuth at each range bin. Following this iterative procedure, it leads to the image in figure (1-19). In figure(1-19), the above-iterative procedure is performed based on dominant scatterer within a very small bandwidth which is $[-6, 6]$ Hz.

The reason to choose a small Doppler interval, is that, since there are several targets which might have almost the same strength but different speed relative to that of radar, the motion compensation for one will result in the smearing for the others, so the image might look a little bit messy, as illus-

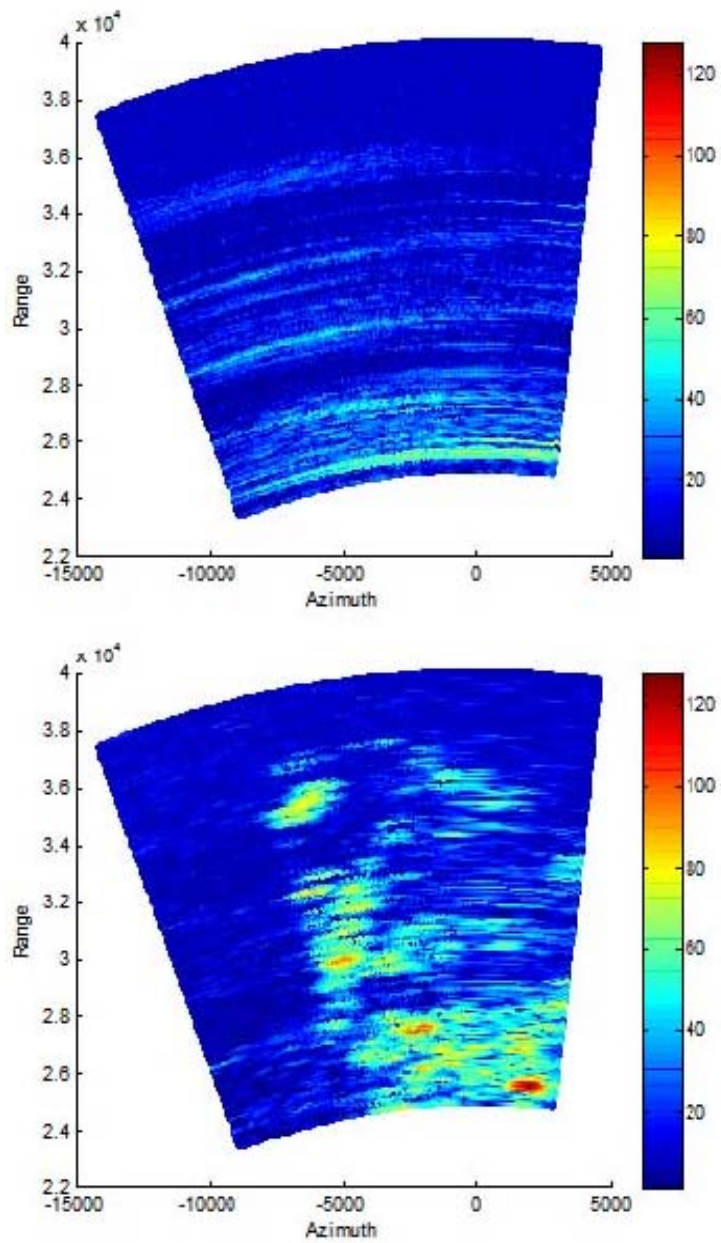


Figure 1.17: Raw(at top) and focused (at bottom) images using the horn antenna

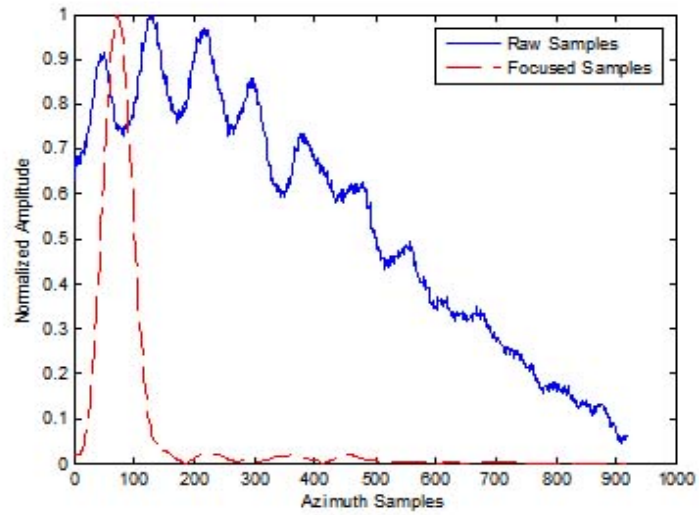


Figure 1.18: Raw and focused azimuth samples at a specific range from horn

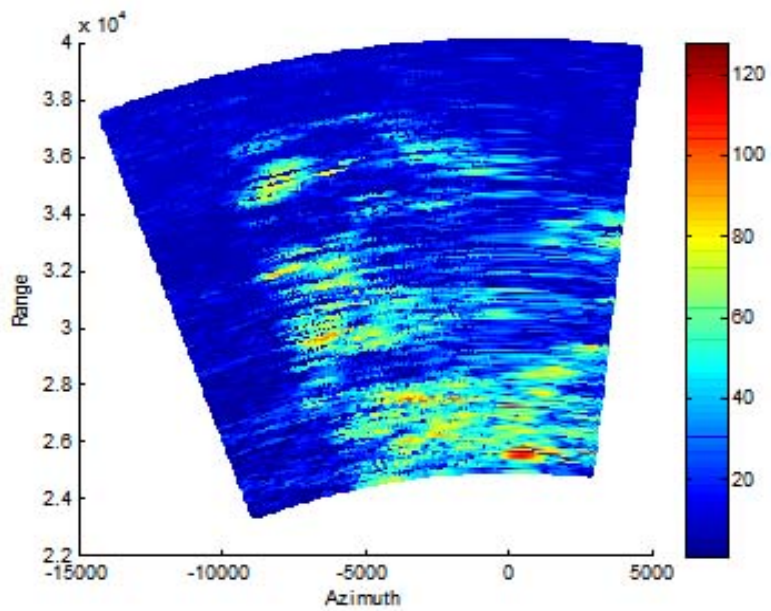


Figure 1.19: Raw and adaptively-focused images from horn

trated in figure (1-20).In this image, the corresponding Doppler bandwidth is within $[-20, 20]$ Hz.

Eventhough one may think that it is better to partition the whole image into smaller blocks and then apply the filter's shifting to each block,here it doesn't do any good and even make it worse becasue first of all the full aperture which is very big is used and second of all the scene contains different targets with different Doppler features,i.e., the scene is quite inhomogeneous. This approach is only going to be taken into analysis for precipitation in the next chapter.

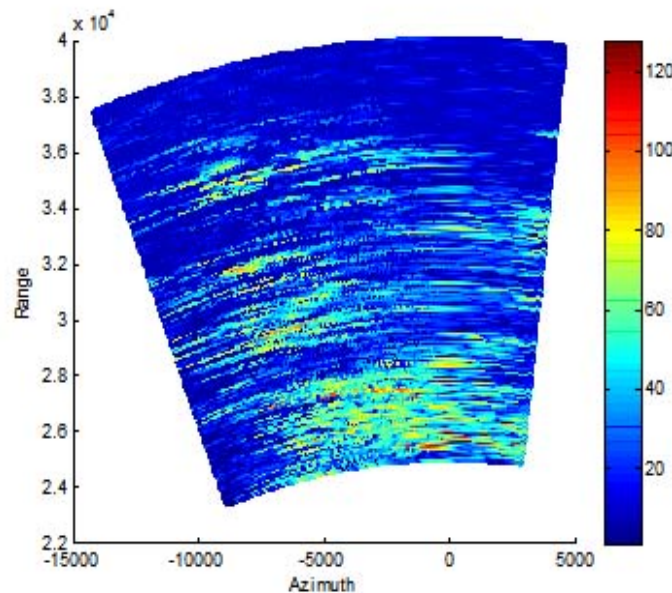


Figure 1.20: Raw and adaptively-focused images from horn

Another alternative would achieve through estimation of the mean Doppler shift of dominant scatterers at each range bin. The figure (1-21) shows the resultant image of the mean motion compensation due to both antenna and targets (here are both clutters and clouds). However; through this adaptive approach, one can find out the true location at least for dominant scatterers. This important fact is apparent in figure (1-22) and (1-23). Two totally different range bins are taken into consideration in these last images. As a consequence, after the SAR processing, the detected target will look shifted

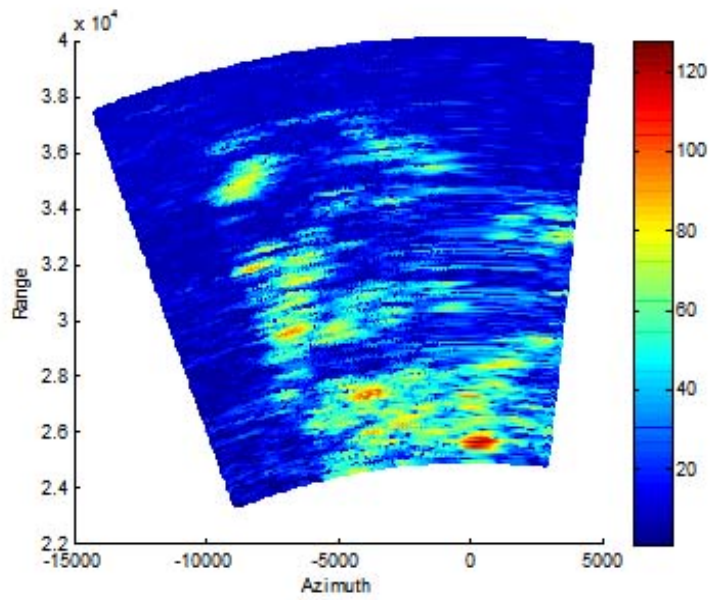


Figure 1.21: Raw and adaptively-focused images from horn

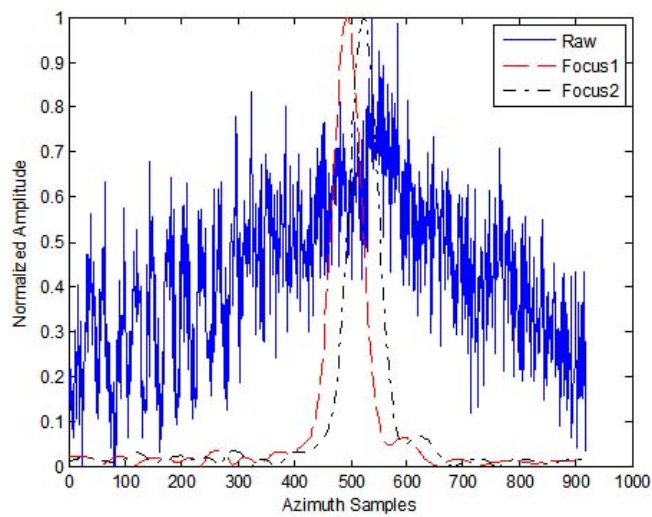


Figure 1.22: Raw, focused (Focus1), and adaptively-focused (Focus2) azimuth samples at a specific range from horn

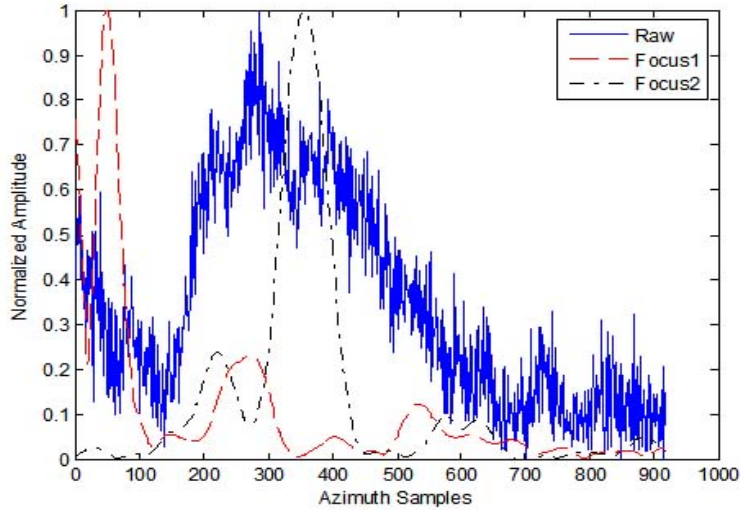


Figure 1.23: Raw, focused (Focus1), and adaptively-focused (Focus2) azimuth samples at a specific range from horn

if the correction of center of the postfilter is disregarded.

Bear in mind that in all images so far, the dynamic range(DR) of the colors are chosen to be the DR of the processed data. In fact if the energy of the post filter is not normalized the noise floor will increase by the factor of $10 \log_{10}(N)$ and the signal power will increase at most by factor of $10 \log_{10}(N^2)$ in dB. Therefore the DR (or SNR) of the focused image compared to the raw image will reach the maximum $10 \log_{10}(N)$ in dB(the maximum occurs for the ideal point target).

1.3 Super-Resolution Strip-map CSAR

In order to gain a high-resolution image with a very good quality (a clean image), a couple of issues must be taken care of. Artifacts introduced by high sidelobe levels even by those quite far away from the main lobe, deteriorate the image quality, even though the first strong sidelobes can be mitigated by windowing/tapering such as hamming window at the cost of resolution. Probably in some applications it is not desired to pay such a cost. On the other hand, in some SAR systems such as the one considered in this thesis,the windowing doesn't suffice to remove the artifacts when a full long aperture is employed in SAR processor to focus a few strong and closely situated scatterers.

To have an idea about how big the sidelobes are after SAR post filter (PF),

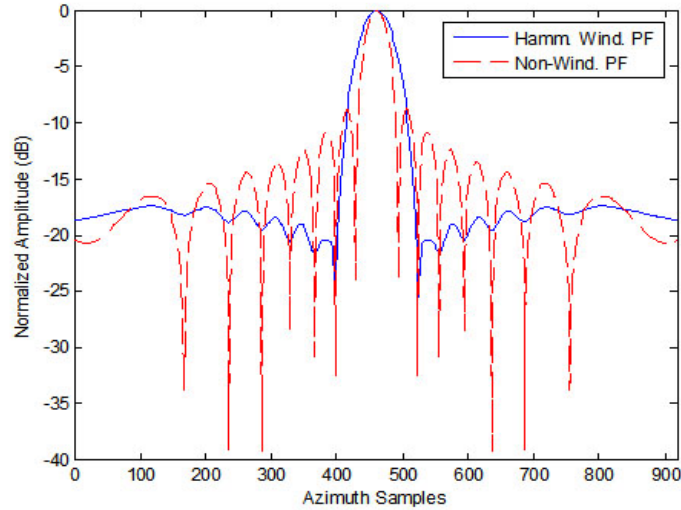


Figure 1.24: Non-windowed and windowed responses of Horn CSAR's post filter

figure(1.24), shows both Non-windowed SAR's response after PF and its windowed counterpart performed by Hamming coefficients.

To get rid of artifacts, a cleaned algorithm first used in phased-array imaging radars by Tsao and Steinberg (1988) is modified and applied to the imaging of clutters extracted by horn. To the best of author's knowledge, the stated algorithm hasn't yet been used for tackling with artifacts caused by SAR's system, instead it was exploited to wipe out the artifacts in phased-array imaging systems by the aforementioned authors who claimed in their paper they haven't yet implement it for SAR imaging.

The flow chart of proposed iterative 2-D CLEANED based algorithm is fully described in figure(1.25). The algorithm is illustrated for 2-D compressed image. However; the processed pattern along azimuth simply attends in sidelobe subtraction step. The two algorithms CLEAN and RELAX are explained in details in the following chapter.

These two algorithms are only used to localized the strongest remaining scatterer along with its corresponding parameters in two dimensions that is range and cross range.

In figure (1.26) images including non-windowed and two CLEANED strip-map CSAR are plotted for the sake of comparison. The iterating procedure is terminated for the first and second CLEANED images when the remaining energy hits about twenty and fifteen percent of that of processed image respectively which is still not quite enough and it is to be further continued. One may also apply threshold condition (Tsao and Steinberg, 1988) to stop

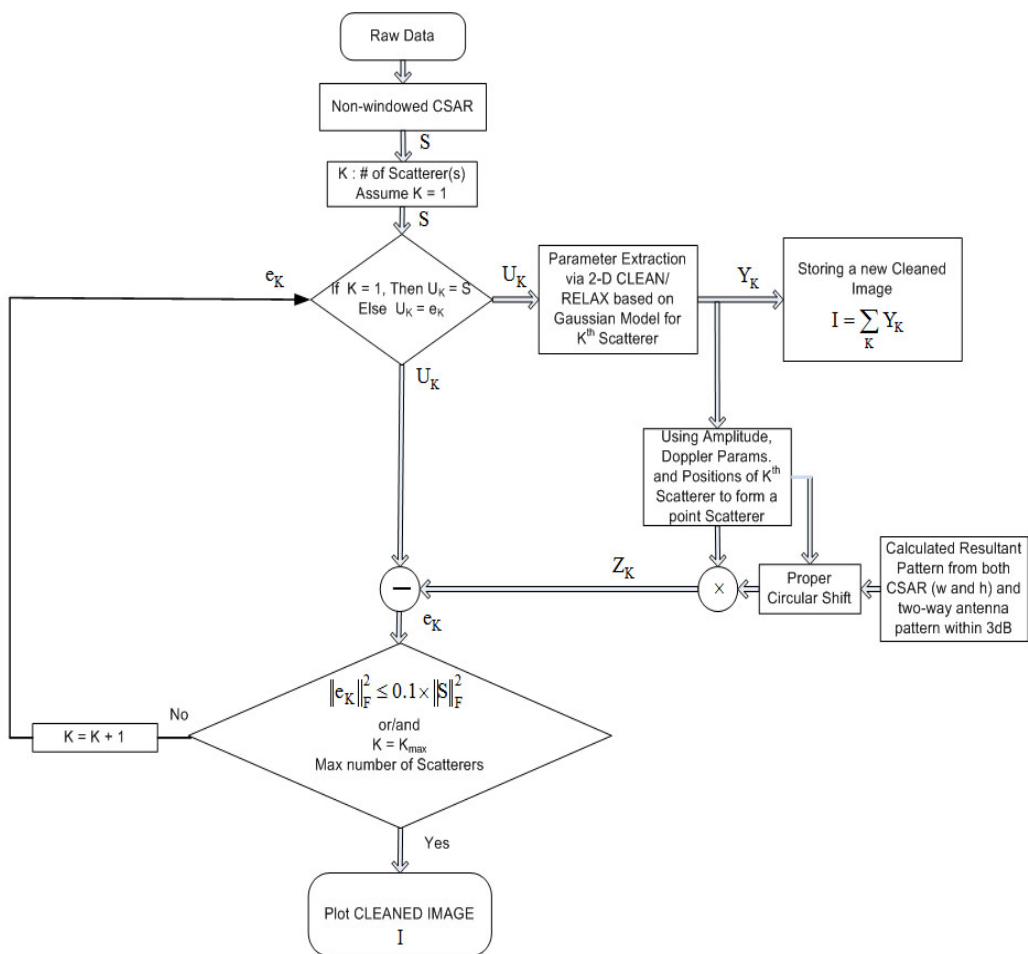


Figure 1.25: Flow chart of CLEANED Strip-map CSAR algorithm

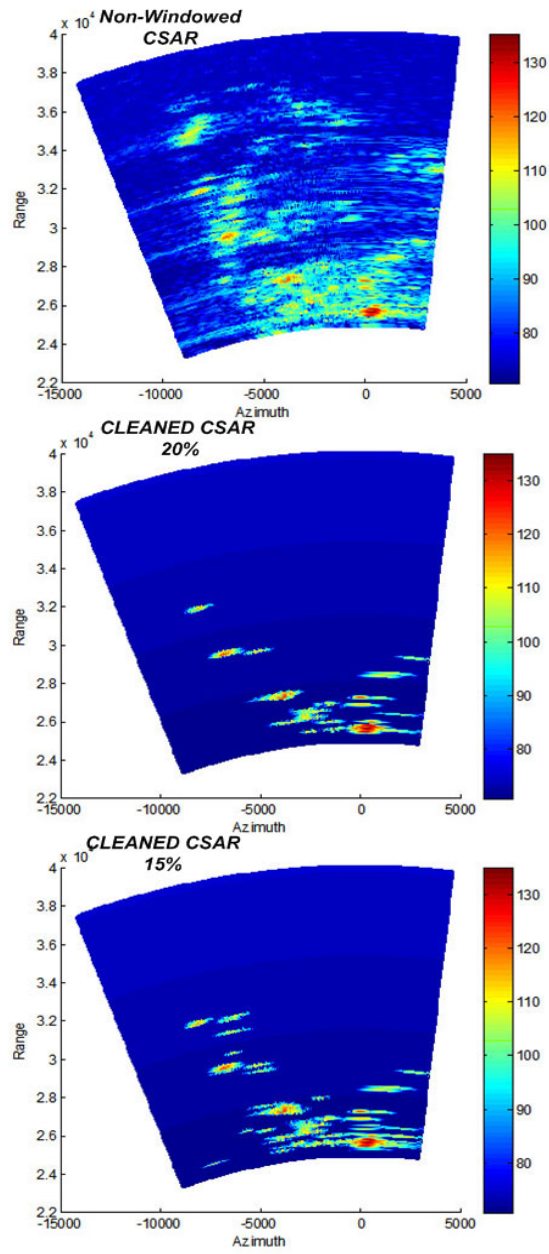


Figure 1.26: Images of CSAR and CLEANED CSAR

the process and thereby regard the rest of energy as a noise or undesired energy in the uncleaned image.

The resolution in this algorithm doesn't degrade in comparison with the non-windowed CSAR. This fact plus the robustness of this algorithm in recognizing and omitting strong artifacts, even those at close proximity to main lobe(s), are depicted in figure (1.27) for azimuth samples at several range bins regarding both non-windowed and CLEANED ground-based strip-map CSAR. In figure (1.27) several different cases obtained from the processed image of clutters, are taken into account to confirm the capability as well as precision of the proposed algorithm.

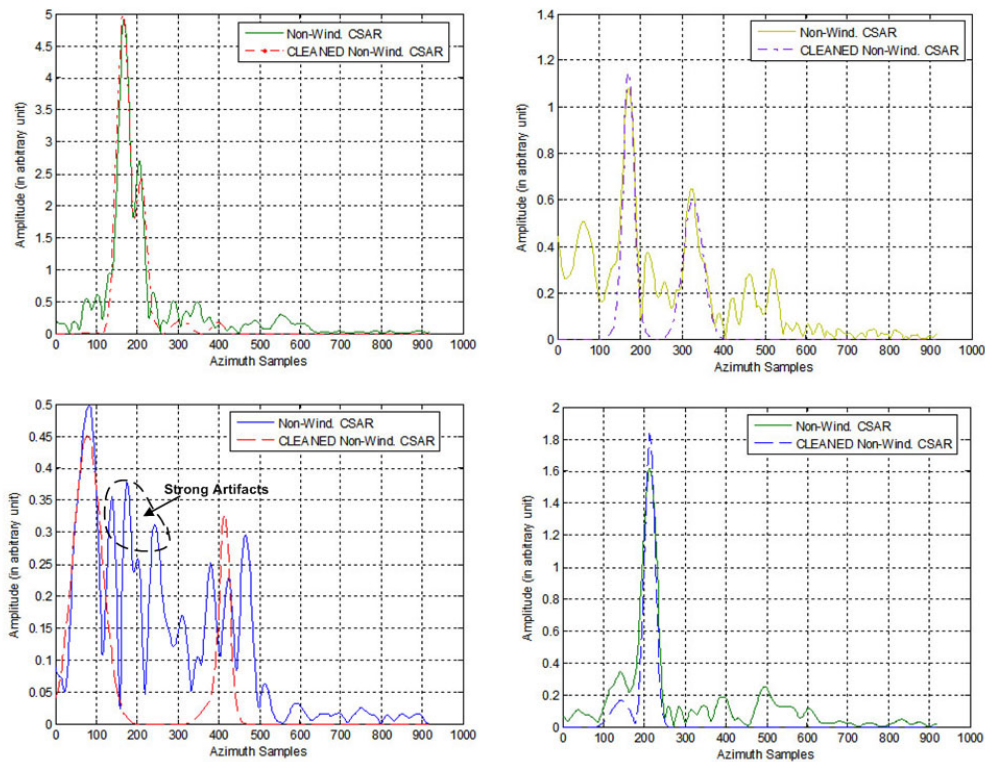


Figure 1.27: Azimuth samples at several range bins of both CSAR and CLEANED CSAR

The key point in this cleaning algorithm is the proper subtraction of correct estimated and well-positioned sidelobes at each iteration. As the pattern specification such as SLL, sidelobe's positions and its width can be severely affected by the nature of the scene such as random or partially coherent scenes, the cleaning algorithm fails to eliminate artifacts and indeed it itself creates false targets in random or partially coherent scenes where the resolution is dominantly determined by target itself rather than SAR system.

Thus, the proposed method is useful and efficient for coherent scene such as those of ground clutters, man-made targets, etc., and it should not be implemented for random scene such as weather targets.

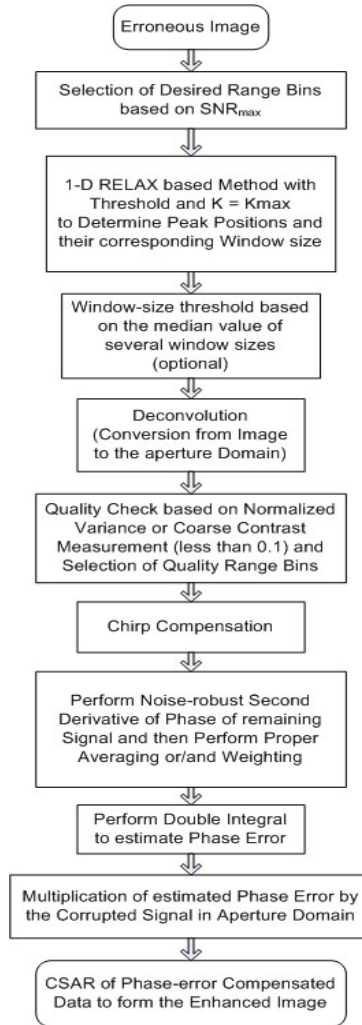


Figure 1.28: Flow chart of strip-map QPGA algorithm

In order to achieve maximum compression the phase error arisen from SAR system and uncompensated motion should be mitigated. Of all several methods for the compensation of range-independent phase error, here two robust algorithms including phase-gradient autofocus (PGA) for both spotlight (or ISAR) (Wahl et al., 1994a) and strip-map SAR mode (Wahl et al., 1994b) and its faster non-iterative quality version i.e., quality phase-gradient autofocus (QPGA) (Chan and Yeo, 1998; Chan and T. S. Yeo, 2002) suggested for only spotlight SAR/ISAR are exploited. Indeed the strip-map

version of QPGA which has not considered before, is realized in this section. However, it is very similar to strip-map version of PGA with some modification performed with the aid of QPGA methodology. The steps of strip-map SAR autofocus based on modified QPGA is described in details in flow chart drawn in figure(1.28).

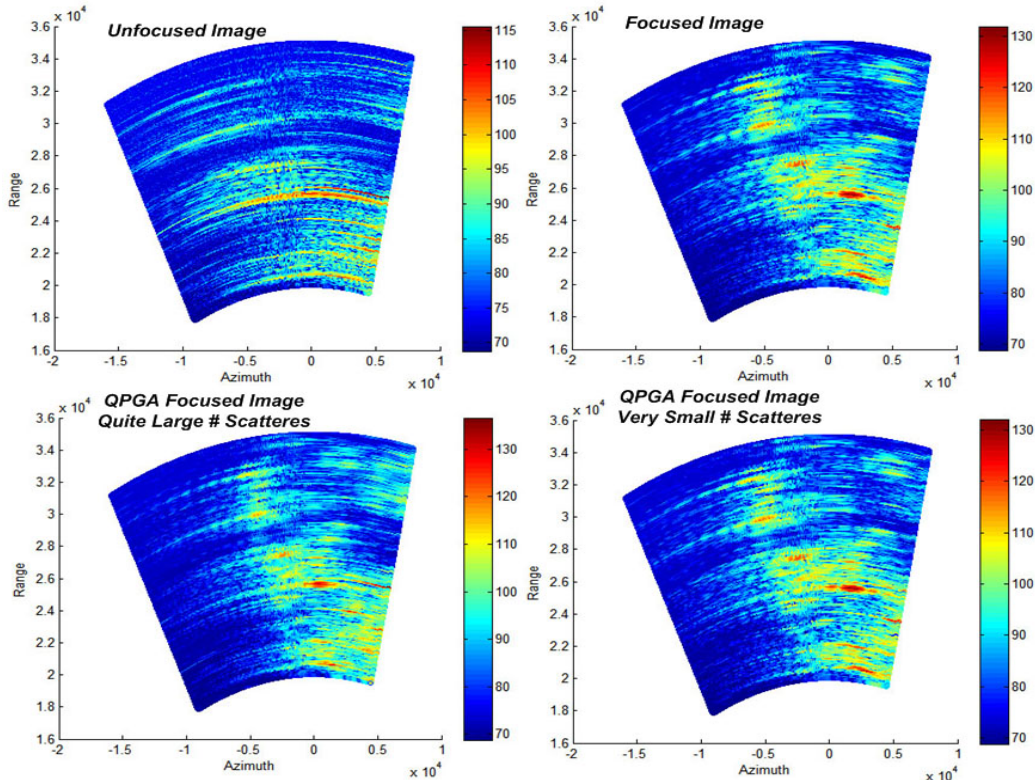


Figure 1.29: Raw, processed and enhanced images by strip-map QPGA algorithm in CSAR

This algorithm and its related counterparts are simply able to mitigate the 1-D phase error which are redundant and repetitive at each chosen range bins (i.e., those in the pool of scatterers). On the other hand those 2-D phase errors, range-dependent phase error, can not be removed unless their fluctuation along range dimension is slow enough as compared to the phase curvature along azimuth thereby might be ignored. In such case, the large image or big swath can be divided into small subswaths (not very small in order to have useful scattering sources) and the phase-error estimation as well as correction is accomplished for each and every subswath separately. A similar approach to this is going to be used for precipitation (random scene) in the next chapter in a limited way. The number of quality range bins as well

as noise robust discrete numerical difference method(s) is crucial to estimate phase error in particular those due to inherent SAR's system distortions. One may employ either the second derivative of linear unbiased minimum variance (LUMV) or that of Knox-Thompson(based on second derivative of higher-order truncation which uses more samples) (Wahl et al., 1994a). Herein the latter one is considered.

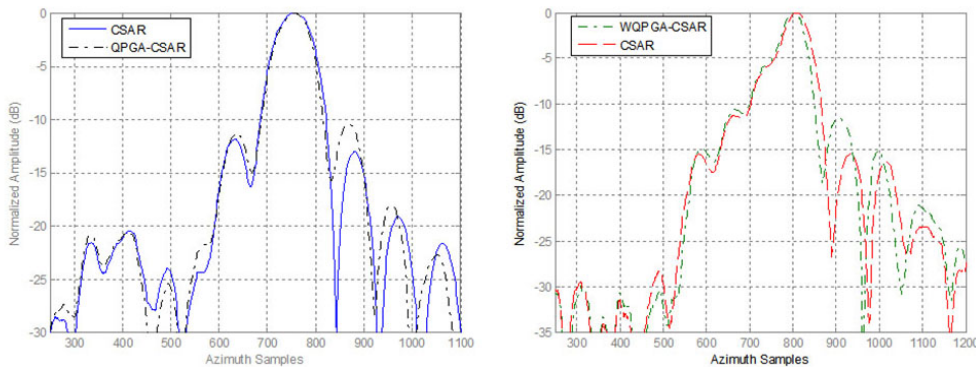


Figure 1.30: Azimuth samples at several range bins of both CSAR and QPGA CSAR for very small pool size

As an example the focus CSAR system is regarded as partially focused and shifted image which can be fixed by above algorithm depending on the pool size of sources. Figure (1.29) shows that the system contains both uncompensated motions and quadratic terms stemming from the CSAR system and after one iteration phase error correction these errors are suppressed considerably thus leads to a higher resolution image. Note that for recognizing the changes more clearly none of the images are windowed to remove sidelobes and their associated artifacts. There exist several criteria including increase in SNR and sidelobe level (SLL) as well and decrease in width of mainlobe, which might be taken for granted to find out the enhancement in the corrected image. For better insight, the processed and corrected azimuth patterns at a few range bins of the regarding example are plotted in figure (1.30) and figure(1.31) for small and quite large pool sizes respectively.

1.4 Concluding Remarks

So far, the results of ground-based CSAR, rotating SAR, for quasi-static targets (non-fade scene and smooth with small velocity compared to the antenna velocity such as ground clutters), the azimuthal resolution can be significantly improved by properly selecting the size of the both antenna and

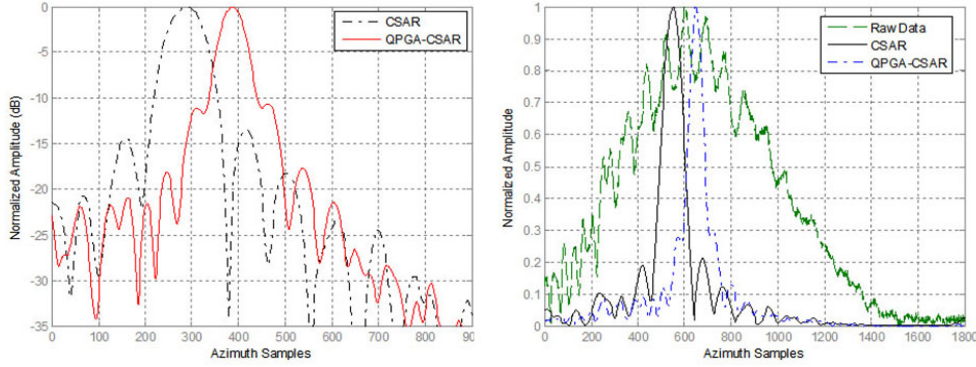


Figure 1.31: Azimuth samples at several range bins of both CSAR and QPGA CSAR for quite large pool size

platform. In other words, the ratio of D/l_h must be high enough to enhance the azimuth resolution for even an ideal point scatterer. Here the speed of the antenna doesn't play the pivotal role provided that the targets are almost stationary with respect to antenna. The reverse will be proven to be true in the next chapter for precipitation imaging.

In this chapter the full synthetic aperture, except for the last section, has taken into process, i.e., the maximum possible integration time which is about 700 ms for horn antenna and is only applicable for point scatterers due to its high correlation time. In fact the maximum derived processing gain is 3dB less than the maximum possible gain obtained for a point scatterer based on a full-synthetic processing. The maximum processing gain in dB for a point scatterer without any windowing in SAR processing and non-unit-energy post filter is given as

$$G_p = 10 \log_{10}(N^2) \quad (1.15)$$

For the unit-energy post filter the maximum would be

$$G_p = 10 \log_{10}(N) \quad (1.16)$$

For both cases the maximum increase in DR is

$$DR = 10 \log_{10}(N) \quad (1.17)$$

To improve the CSAR resolution along with elimination of artifacts without incurring any loss in resolution for coherent scene, one can bring both cleaning and phase-error mitigation algorithms into SAR processing after post filter as a post processor. However the larger the number of iterations

or/and presumed number of dominant scatterers the less the improvement of the quality. In other words the cleaning method is really slow for large scenes such as the one regarded in the corresponding example.

Chapter 2

Ground-based PSAR

2.1 Precipitation Imaging

In this chapter, the goal is to try to focus the data from precipitation (by precipitation, it is meant to be rain) in order to improve the azimuthal resolution in the image. Furthermore; as in Doppler weather radar the resolution volume is of great significance in estimation of volume reflectivity as well as rain rate, the increase in the resolution volume make a better and more reliable estimation of these parameters.

Similar to the previous chapter, herein two different antennas , which are parabolic reflector and standard horn antennas situated back to back on the same pedestal as shown in figure (2.1), are used. Before we start with precipitation imaging, it's noteworthy to go through some important facts in weather targets in order to understand specifications of the target scene and its behavior in terms of SAR.

Meteorological targets are distributed and moving in a random way due to several factors, such as turbulence, wind shear, and spread of particle fall speed. These factors alter the phase of the received signal in a noise-like manner especially in the severe weather condition. Moreover; the wind speed varies with height within a three dimensional precipitation cell/area. Indeed the volume nature of the target and its internal motions adds more phase variation besides the large-scale motions such as horizontal wind across the azimuth (the desired dimension). In addition to these sources of phase error/fluctuation, propagation anomalies also cause phase propagation errors(Brown and Riordan, 1970). The phase fluctuation results in both Doppler shift and Doppler spread in the spectrum of the received data along azimuth (Atlas et al., 1977; Greene and R.T.Moller, 1962).

The resultant phase error from meteorological phenomena on the received



Figure 2.1: Reflector and Standard Horn antennas, Courtesy of SELEX-SI Gematronik Co.

data, might limit the capability of SAR so drastically. In other words the maximum obtainable gain and resolution of SAR turn out to be severely degraded by this phase error across the synthetic array. The amount of deterioration strongly depends on the variance of the phase error (apart from the systematic phase error induced by SAR prefilter) (Metcalf and Holm, 1979). From array pattern's point of view, the increase in the rms of the phase error makes the process gain drop severely thus the half power beamwidth becomes wider. Besides, the sidelobe level (SLL) gets worse (Greene and R.T.Moller, 1962) which can lead to artifacts such as breakup in desired signals as well as detection of false target(s) (Tsao and Steinberg, 1988).

According to the discussion so far, some preprocessing steps are required prior to SAR postfiltering or postprocessing, as it is known to be a LPF. Unlike, spaceborne-based and airborne-based SARs, the postfilter of ground-based SAR has quite narrow Doppler bandwidth particularly due to its small velocity compared to its very fast-moving counterparts. The corresponding bandwidth is in the order of few hertz versus that of air/space-borne-mounted SAR which is about a few hundred hertz or even wider. It will be understood later on that this is the most restrictive parameter on ground-based PSAR. Thus either two parameters of the postfilter ,i.e., frequency center and bandwidth of the filter as well, are to be adjusted or equivalently the speed and other high-order motion which manifests phase error, of the target(s) must be compensated before passing through the SAR's postfilter.

As a result, in the following subsections some signal processing algorithms

exploited for these purposes are going to be described in some details.

2.1.1 Doppler Spectrum Estimation

The proper estimation of either Doppler velocity center or Doppler frequency center as well as Doppler spread is of great concern not only for meteorological purpose but also for SAR analysis of scene containing moving targets like precipitation.

The conventional approach(es) of first and second moments of Doppler spectrum, such as pulse-pair estimator (PP) and direct fast Fourier transform (FFT) is more reliable under some circumstances and assumptions including high SNR (usually larger than 20 dB), Gaussian spectrum (considerable deviation from Gaussian shape can frequently occur(Janssen and Vanderspek, 1985)), and symmetrical as well as narrow spectrum width (normally up to about 0.4 times the Nyquist velocity, v_a) (Doviak et al., 1979).

Other methods such as Burg's maximum entropy,Prony, Pisarenko (Kay and Marple, 1981),Music for Doppler weather radar (Chen et al., 1995) (eigendecomposition-based methods) , noise compensated autoregressive(AR) method (based on white noise and priori knowledge of its variance)(Kay, 1980), linear prediction (LP) which is regarded as a generalized PP efficient at high SNR (larger than 20dB),minimum-norm (MN, based on eigendecomposition of LP equation useful at lower SNR versus LP, however; not reliable at SNR lower than 10dB)(Banjanin et al., 1993),vector and poly-pulse pair estimation (taking higher-order lags of autocorrelation in mean velocity estimation versus one-lag PP processor)(Mahapatra and Zrnic, 1983; Lee, 2000) which is supposed to compensate for the bias error due to assumption of narrow and symmetrical shape of Doppler spectrum,and maximization of the periodogram(spectral method based on FFT)(Mahapatra and Zrnic, 1983), are all considered to be under some other priori assumptions on modeling of weather signal or noise such as AR process of some desired order (all-pole assumption),white gaussian noise or some specific colored noise ,e.g. noise of AR process of some pre-assumed order.

To make a more reliable estimation of Doppler parameters at low SNR, particularly for standard horn case, at fast angular velocity (similarly low number of samples which happens in case of fast-rotating antenna with very small HPBW such as that of reflector),and in general non-Gaussian asymmetrical wide Doppler spectrum which is frequently encountered on the available data sets,herein both CLEAN(Tsao and Steinberg, 1988) and RELAX(complex/iterative version of CLEAN, can be referred to as SUPER CLEAN)(Li and Stoica, 1996) algorithms in one and two dimensions are going to be implemented in a way according to our needs. It is also interesting

to know that the RELAX is robust to mismodeling for noise parameters estimation (insensitive to the assumed AR's order). However; the noise parameter estimation is beyond our purpose which is SAR focusing, and therefore it will be disregarded. The most emphasis is on target feature extraction i.e., Doppler center and Doppler spread of the desired targets by means of RELAX through nonlinear least squared(NLS)technique(Liu and Li, 1998) and trihedral and dihedral models for target(s). Note that the trihedral and dihedral models are robust model for many man-made targets and because of that they have been used in obtaining super resolution SAR imaging (Bi et al., 1999) however; it can be employed to describe a bunch of homogeneous and closely located targets (distributed targets) such as rain drops,the model is tested for both weather targets and clutters in order to simulate the raw data and the corresponding results prove its capability for such natural targets.

Here, first the algorithm for one-dimensional RELAX based on dihedral model is described and then we will proceed with two-dimensional CLEAN algorithm using two-dimensional dihedral model (you may find details of 2-D CLEAN using trihedral or point- scatterer model in (Li et al., 2001)).

1-D RELAX :

In this algorithm the 1-D data sequence along azimuth, $y(R_n, m)$, at a fixed range bin is taken into analysis. For the sake of brevity, the argument R_n is ignored in the following formulation. The input sequence $y(m)$ is described as follows

$$y(m) = s(m) + v(m) \quad m = 0, 1, \dots, M - 1 \quad (2.1)$$

where

$$s(m) = \sum_{k=1}^K \alpha_k \text{sinc}[PRI\Delta_{a_k}(m - d_{a_k})] \exp(j2\pi PRI m f_{a_k}) \quad (2.2)$$

M is the length of the input vector and $\text{sinc}(x) = \sin(\pi x)/\pi x$.

The goal is to estimate unknown parameters $\{\alpha, \Delta_a, d_a, f_a\}$ representing the features of the target(s) through minimizing the NLS cost function C_1

$$C_1(\{\alpha_k, \Delta_{a_k}, d_{a_k}, f_{a_k}\}_{k=1}^K) = \|\mathbf{y} - G\boldsymbol{\alpha}\|^2 \quad (2.3)$$

where

$$\mathbf{y} = [y(0) \quad y(1) \quad \dots \quad y(M - 1)]^T \quad (2.4)$$

$$\boldsymbol{\alpha} = [\alpha_1 \quad \alpha_2 \quad \dots \quad \alpha_K]^T \quad (2.5)$$

$$G = [\mathbf{g}(0) \quad \mathbf{g}(1) \quad \dots \quad \mathbf{g}(M - 1)]^T \quad (2.6)$$

$$\mathbf{g}(m) = [g_1(m) \quad g_2(m) \quad \dots \quad g_K(m)]^T \quad (2.7)$$

in which

$$g_k(m) = \text{sinc}[PRI\Delta_{a_k}(m - d_{a_k})] \exp(j2\pi PRImf_{a_k}) \quad (2.8)$$

“T” and “ $\|\cdot\|$ ” denote transpose and Euclidean norm respectively. “K” is the maximum number of targets(both point and distributed ones) determined automatically by the algorithm itself via generalized Akaike information criterion(GAIC) (Li and Stoica, 1996). minimizing the C_1 with respect to α gives its estimate $\hat{\alpha}$

$$\hat{\alpha}_k = \frac{G_k^H \mathbf{y}}{G_k^H G_k} \quad (2.9)$$

“H” stands for Hermitian matrix operation. G_k is the kth column of G. “ $\hat{\cdot}$ ” denotes estimates.

By inserting equation (2.9) into equation (2.3) and doing some simplification, the minimization of C_1 will end up with maximization of the following new cost function, C_2

$$C_2(\Delta_a, f_a, d_a) = \frac{|G^H \mathbf{y}_k|^2}{G^H G} \quad (2.10)$$

in which \mathbf{y}_k is

$$\mathbf{y}_k = \mathbf{y} - \sum_{i=1, i \neq k}^K \alpha_i \mathbf{g}_i \quad (2.11)$$

The above maximization requires a three-dimensional search over three remainder parameters. To solve this, an alternating maximization procedure(Liu and Li, 1998) which updates one parameter estimate by fixing the other two. Notice that when two parameters, Doppler spread and delay time, are kept fixed the Doppler frequency, f_{a_k} is readily estimated by finding the dominant peak in 1-D fast Fourier transform (FFT) with enough zero padding in order to have a precise estimation. Thus

$$\hat{f}_{a_k} = \text{arg max}\{FFT\{\frac{|Mult(\mathbf{g}_k(f_{a_k} = 0), \mathbf{y}_k)|^2}{\mathbf{g}_k^H(f_{a_k} = 0)\mathbf{g}_k(f_{a_k} = 0)}\}\} \quad (2.12)$$

“Mult(\mathbf{x}, \mathbf{y})” defines as element-by-element multiplication of two vectors \mathbf{x} and \mathbf{y} with equal length.

Employing the above-mentioned equations the iteration steps of 1-D RELAX are as following

Step(1): Assume $K = 1$. Determine the first estimate of four parameters of the first dominant scatterer, i.e. $\{\hat{\Delta}_{a_1}, \hat{f}_{a_1}, \hat{d}_{a_1}, \hat{\alpha}_1\}$ from \mathbf{y} as described above.

Step(2): Assume $K = 2$. Compute \mathbf{y}_2 with equation (2-11) by using estimated parameters calculated in step(1).

From that, the parameters $\{\hat{\Delta}_{a_2}, \hat{f}_{a_2}, \hat{d}_{a_2}, \hat{\alpha}_2\}$ of the second dominant scatterer are obtained. Next, compute \mathbf{y}_1 with (2-11) by using $\{\hat{\Delta}_{a_2}, \hat{f}_{a_2}, \hat{d}_{a_2}, \hat{\alpha}_2\}$ and then redetermine $\{\hat{\Delta}_{a_1}, \hat{f}_{a_1}, \hat{d}_{a_1}, \hat{\alpha}_1\}$ from \mathbf{y}_1 .

Continue this iterative procedure at this step until the practical convergence, explained later, occurs.

Step(3): Assume $K = 3$. calculate \mathbf{y}_3 with equation (2-11) by taking $\{\hat{\Delta}_{a_i}, \hat{f}_{a_i}, \hat{d}_{a_i}, \hat{\alpha}_i\}_{i=1}^2$ estimated at the end of step(2). Obtain $\{\hat{\Delta}_{a_3}, \hat{f}_{a_3}, \hat{d}_{a_3}, \hat{\alpha}_3\}$ from \mathbf{y}_3 as before. Next, compute \mathbf{y}_1 by using $\{\hat{\Delta}_{a_i}, \hat{f}_{a_i}, \hat{d}_{a_i}, \hat{\alpha}_i\}_{i=2}^3$ via equation (2-11).

Then compute \mathbf{y}_2 with equation (2.11) by using $\{\hat{\Delta}_{a_i}, \hat{f}_{a_i}, \hat{d}_{a_i}, \hat{\alpha}_i\}_{i=1,3}$. Iterate these three substeps until the practical convergence is reached.

Step($k > 3$): Continue similarly until k is equal to K which is determined by GAIC explained below.

Practical convergence in the iterative process above may be determined by checking the relative change in the cost function $C_1(\{\hat{\alpha}_k, \hat{\Delta}_{a_k}, \hat{d}_{a_k}, \hat{f}_{a_k}\}_{k=1}^K)$ in equation (2.3) between two consecutive iterations to make sure it becomes less than a certain value for instance 10^{-4} .

K is determined as the integer that minimize the following GAIC cost function.

$$GAIC_K = M \ln(\|\mathbf{e}\|^2) + 4 \ln(\ln M) (3K + 1) \quad (2.13)$$

where the error vector \mathbf{e} is defined as

$$\mathbf{e} = \mathbf{y} - \sum_{k=1}^K \alpha_k \mathbf{g}_k \quad (2.14)$$

2-D CLEAN :

CLEAN is a faster and less complex version of RELAX with less accuracy of course. Basically those iterative substeps stated in RELAX algorithm are avoided in CLEAN algorithm.

Following almost the same procedure as above in two dimensions and assuming K dominant scatterers, the received signal in two dimensions i.e., range and cross-range is

$$y(m, \bar{m}) = s(m, \bar{m}) + v(m, \bar{m}) \\ m = 0, 1, \dots, M - 1 \quad , \quad \bar{m} = 0, 1, \dots, \bar{M} - 1 \quad (2.15)$$

$$s(m, \bar{m}) = \sum_{k=1}^K \alpha_k \text{sinc}[PRI \Delta_{a_k} (m - d_{a_k})] \exp(j2\pi PRI m f_{a_k}) \times \\ \times \text{sinc}[RSI \Delta_{r_k} (\bar{m} - d_{r_k})] \exp(j2\pi RSI \bar{m} f_{r_k}) \quad (2.16)$$

\mathbf{y}, \mathbf{s} , and \mathbf{v} denote $M \times \bar{M}$ matrices in which M and \bar{M} are number of samples along azimuth and range respectively.

The NSL estimates of target(s) features are obtained via minimizing cost function C_1

$$C_1(\{\alpha_k, \Delta_{a_k}, d_{a_k}, f_{a_k}, \Delta_{r_k}, d_{r_k}, f_{r_k}\}_{k=1}^K) = \|\mathbf{y} - \sum_{k=1}^K \mathbf{G}_k \alpha_k\|_F^2 \quad (2.17)$$

where “ $\|\cdot\|_F$ ” denotes the Frobenius norm and

$$\mathbf{G}_k = \mathbf{g}_a \times \mathbf{g}_r^T \quad (2.18)$$

$$\mathbf{g}_a = [g_a(0) \quad g_a(1) \quad \cdots \quad g_a(M-1)]^T \quad (2.19)$$

$$\mathbf{g}_r = [g_r(0) \quad g_r(1) \quad \cdots \quad g_r(\bar{M}-1)]^T \quad (2.20)$$

$$g_a(m) = \text{sinc}[PRI\Delta_{a_k}(m - d_{a_k})] \exp(j2\pi PRI m f_{a_k}) \quad (2.21)$$

$$g_r(\bar{m}) = \text{sinc}[RSI\Delta_{r_k}(\bar{m} - d_{r_k})] \exp(j2\pi RSI \bar{m} f_{r_k}) \quad (2.22)$$

Minimizing C_1 in equation (2.17) with respect to α_k leads to

$$\alpha_k = \frac{\mathbf{g}_a^H \mathbf{y}_k \bar{\mathbf{g}}_r}{\|\mathbf{g}_a\|^2 \|\bar{\mathbf{g}}_r\|^2} \quad (2.23)$$

where

$$\mathbf{y}_k = \mathbf{y} - \sum_{i=1, i \neq k}^K \mathbf{G}_i \alpha_i \quad (2.24)$$

By inserting equation(2.23) into equation(2.17) and doing some simplification, the minimization of C_1 can be performed by maximization of the following new cost function

$$C_2(\Delta_{a_k}, d_{a_k}, f_{a_k}, \Delta_{r_k}, d_{r_k}, f_{r_k}) = \frac{\|\mathbf{g}_a^H \mathbf{y}_k \bar{\mathbf{g}}_r\|^2}{\|\mathbf{g}_a\|^2 \|\bar{\mathbf{g}}_r\|^2} \quad (2.25)$$

To maximize the last equation, a six-dimensional search over the parameter space is required. Similar to the RELAX, an alternating maximization procedure which is to update the parameters $\{f_a, f_r\}, \Delta_a, d_a, \Delta_r, d_r$ while fixing the remaining parameters, is taken into account. Note that for some given parameters $\Delta_a, d_a, \Delta_r, d_r$ the denominator of equation (2.25) is constant. Therefore the estimate of frequency pair $\{f_a, f_r\}$ is determined by maximizing $|\mathbf{g}_a^H \mathbf{y}_k \bar{\mathbf{g}}_r|$ which can be efficiently calculated via 2-D FFT with enough zero padding in both dimensions for better accuracy.

Employing the above-mentioned equations the steps of 2-D CLEAN are as

following

Step(1): Assume $K = 1$. Obtain the estimate of the parameters of the first dominant scatterer, i.e., $\{f_{a_1}, f_{r_1}\}, \Delta_{a_1}, d_{a_1}, \Delta_{r_1}, d_{r_1}$, and α_1 from \mathbf{y} using 2-D FFT, 4-D alternative search and equation (2.23) respectively.

Step(2): Assume $K = 2$. Compute \mathbf{y}_2 with equation(2.24) by using parameters estimated in previous step. Then determine the new parameters of second dominant scatterer which are $\{f_{a_2}, f_{r_2}\}, \Delta_{a_2}, d_{a_2}, \Delta_{r_2}, d_{r_2}$, and α_2 from \mathbf{y}_2 through the same expressions and similar search as above.

Step(3): Assume $K=3$. Calculate \mathbf{y}_3 with equation(2.24) by using parameters estimated in two previous steps. Then estimate the new parameters as done before.

Step($k > 3$): Continue similarly until k is equal to the desired K .

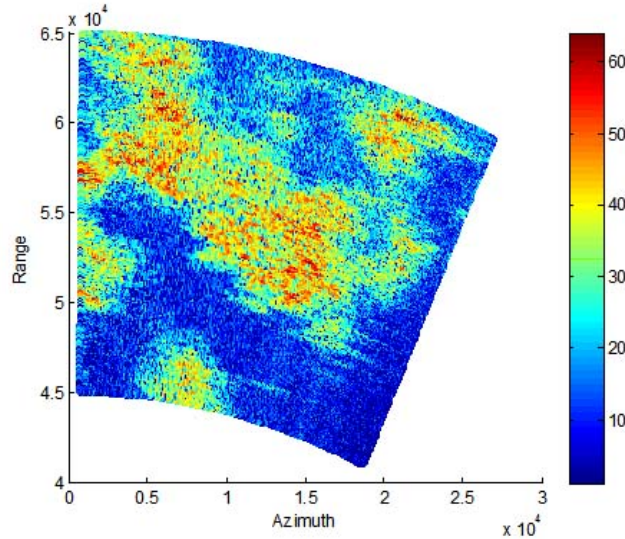


Figure 2.2: Ground-clutter filtered raw data from reflector in rain

In determination of the spectrum width one can also use Gaussian function instead of the sinc function. The results are almost the same but even better for the simulation of the weather targets.

To speed up the process the simple and fast FFTB algorithm(Liu and Li, 1998) extended to two dimensions, are applied to the 2-D CLEAN in order to estimate two parameters, Δ_a, Δ_r . Thus simply a 2-D search for estimation of parameters d_a, d_r is required since the other two parameters $\{f_{a_2}, f_{r_2}\}$ are already determined by 2-D FFT.

Unlike that of RELAX, the K (maximum number of dominant scatterers) is arbitrary selected at the start of the algorithm. Besides, one might set an amplitude threshold with respect to the most dominant scatterer in order to

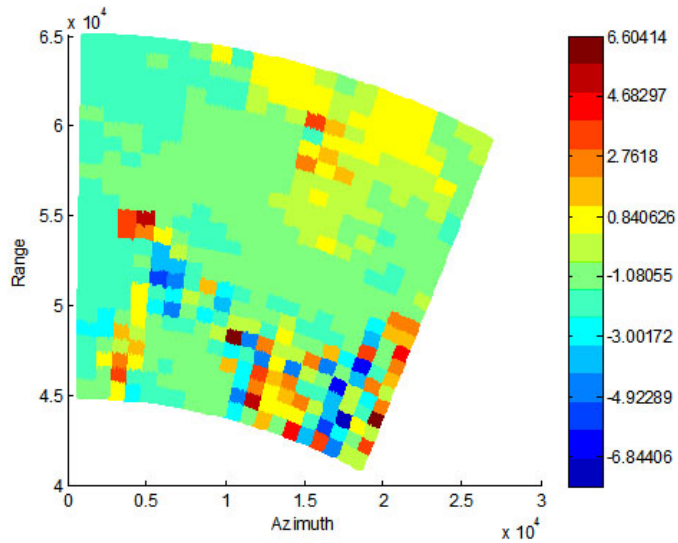


Figure 2.3: Doppler velocity(m/s) of data from reflector in rain

limit the maximum possible K and therefore lower the load of computation. This approach is considered here for both algorithms. 2-D CLEAN can also be replaced by 2-D RELAX with above model at the expense of complexity and computational burden.

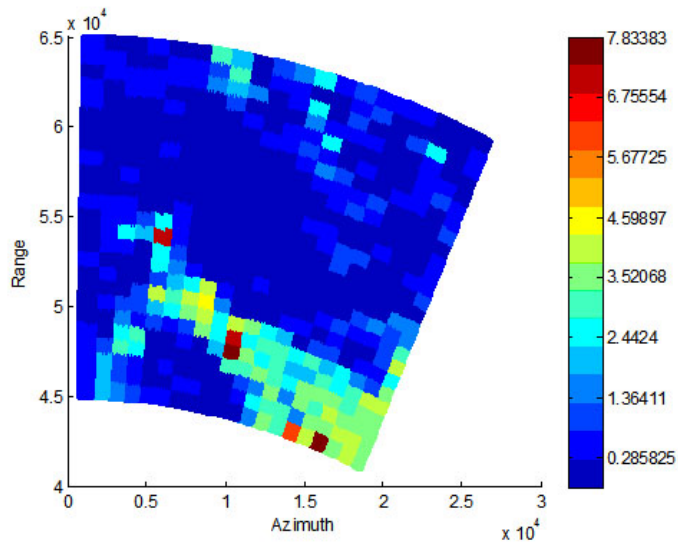


Figure 2.4: Doppler spectrum width (m/s) of data from reflector in rain

Doppler velocity center as well as Doppler spread for two systems, i.e., horn and reflector, in a moderate rain by using 2-D CLEAN are illustrated in the

following plots. Note that the total spectrum widths are estimated which means all the mechanisms contributing to velocity spectrum broadening, such as wind shear, turbulence, antenna rotation, and different drop size fall speeds (Doviak et al., 1979), are included in the corresponding results.

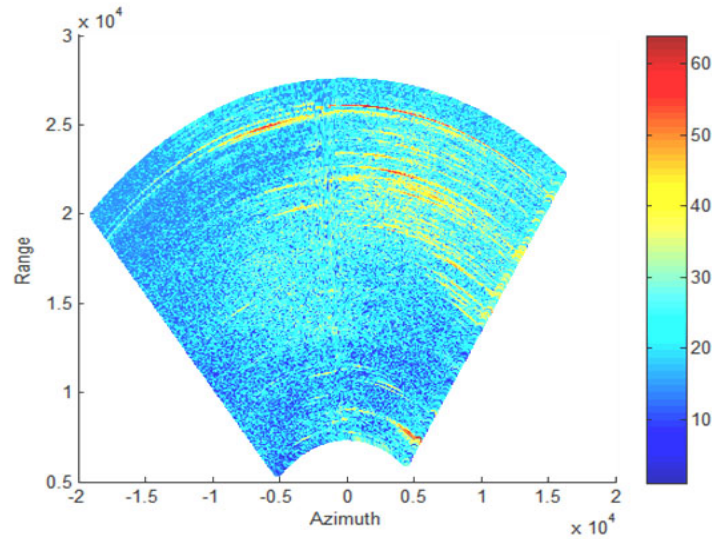


Figure 2.5: Ground-clutter filtered raw data from horn in rain

It is important to know that the ground clutters are removed from the data by zero forcing in Doppler domain (the simplest way to remove the ground clutter is to put zero on frequency samples of data around zero frequency within a certain interval, lets say $[-25 \ 25]$ Hz).

Figures(2.2), (2.3), and (2.4) show the image (normalized amplitude in dB), corresponding Doppler speed and Doppler spectrum width in m/s from reflector in moderate rain, respectively.

Similarly, the image (normalized amplitude in dB), corresponding Doppler speed and Doppler spectrum width in m/s from horn in moderate rain, are demonstrated in figures(2.5), (2.6), and (2.7) respectively.

After the correction of Doppler spectrum width due to both angular velocity of antenna and difference in fall-speed whose Doppler spread occurs due to different drop size and non-zero elevation angle, the residue of Doppler width is attributed to wind shear and turbulence which can be used as a measure to localization of hazardous or severe weather phenomena. The cumulative probability of the corrected results for reflector and horn are depicted together in figure(2.8).

Note that , in the estimation of spectrum width above, the definition of width based on 3dB(half power) has been taken into consideration and the regions

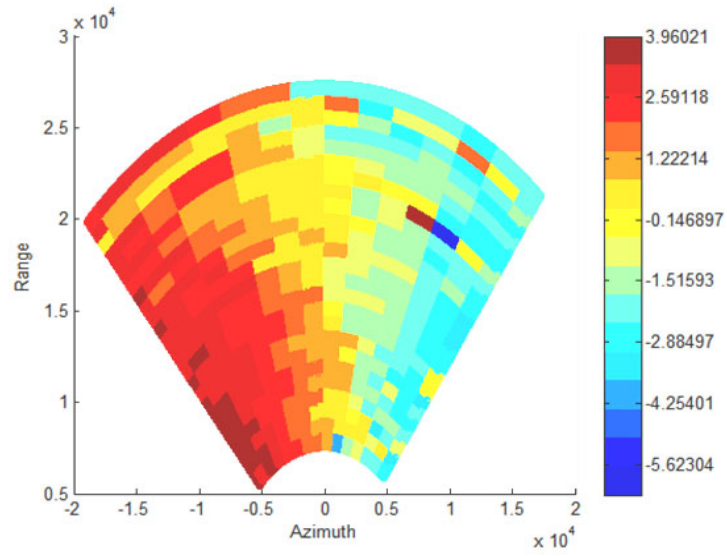


Figure 2.6: Doppler spectrum width (m/s) of data from horn in rain

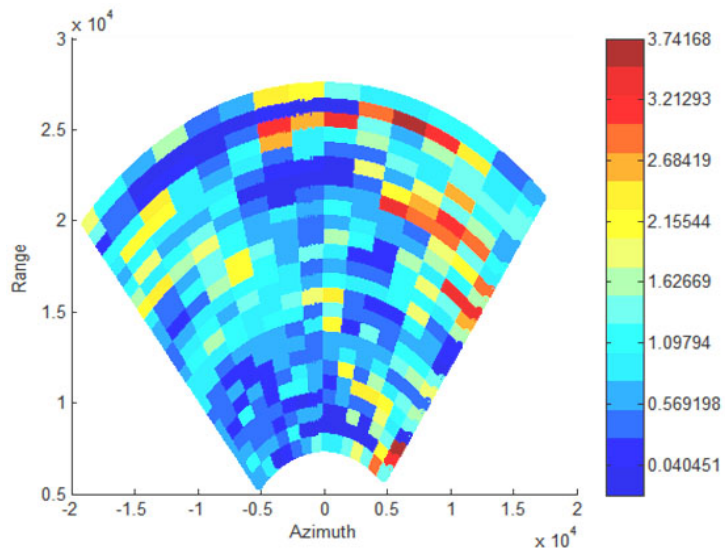


Figure 2.7: Doppler spectrum width (m/s) of data from horn in rain

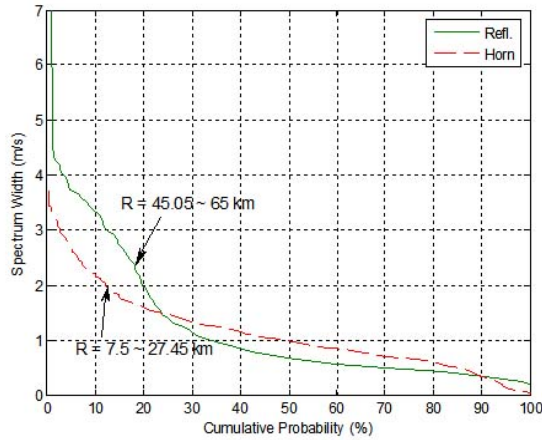


Figure 2.8: Cumulative probability versus corrected spectrum width of data from horn and reflector in quite moderate rain

in which the estimation are performed, are different in both size and range (as well as height) for the two systems. Moreover; the Doppler parameters are determined irrespective of the SNR, so in some cases it is perceivable that the width becomes unexpectedly and abruptly large which might be due to either biases and large variance stems from the low SNR in that regarding areas or high wind shear and turbulence or even due to biological targets such as insects, birds, etc, during the time of observation.

To make the estimate more consistent, one must perform an averaging along both azimuth and range for a few adjacent cells. The mean values of spectrum widths for both antennas in those illustrated regions are about 1.2 m/s which means the rain is quite moderate and weather condition is not severe. However; according to the probability distribution depicted in figure (2.8) the median values are quite different. That for the reflector is about 0.65 m/s and that of horn is about 0.97 m/s.

The reasons of such discrepancies in the results are mainly due to both different heights of experiments and also completely different sizes of volumes containing precipitation because of different resolution sizes in both horizontal and vertical directions but not in slant range. The wind shear and turbulence usually increases by height in a unknown manner which result in widening Doppler spectrum.

Finally, it's worth to give an example of implementation of the CLEAN or RELAX in sidelobe-effect reduction which introduces strong artifacts from the strong clutters particularly ground clutter on the image. These sidelobe artifacts may have destructive impact on the desired signal. In other words they can cause breakup in the desired target area considerably (Tsao and

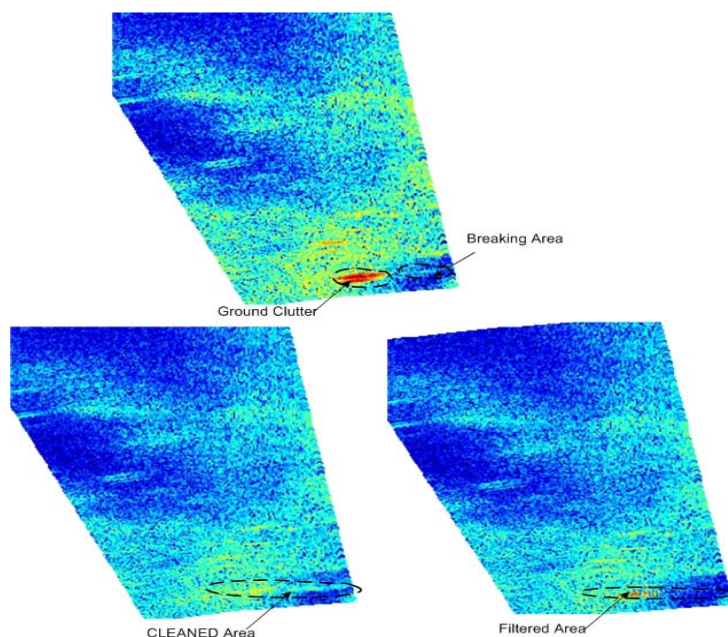


Figure 2.9: CLEANING versus filtering of a very strong ground clutter from reflector in rain

Steinberg, 1988). To perform the removal of this artifact we need to know the radiation pattern along azimuth or its estimate in order to model it and insert it as an amplitude pattern in the CLEAN or RELAX algorithm. Besides, the cleaning approach circumvents the impacts which filtering has on both phase and amplitude of the desired signals at the cost of computation. However; this approach is suitable for point scatterers or a group of point scatterers like those of ground clutters. Figure (2.9) demonstrates this impact on rain area and its recover from ground clutter based on a rough model of the antenna pattern in azimuth.

2.1.2 Autofocusing (Motion Compensation, Phase Error Mitigation and Range Migration Correction)

As mentioned earlier, our desired targets are moving with different velocities which likely might be under sudden changes due to several phenomena. The first thing that must be done is to compensate for the linear motion or equivalently shift the center of the post filter to an appropriate frequency. Either way results in the same outcome. The main problem here is the high fluctuation of velocity from one small area to another, depending on weather condition and the area under imaging, which makes its influence too difficult and complicated to be compensated for within a large area. Thereby,

the whole image is first partitioned into smaller areas uniformly (it can be done in a non-uniform way based on adaptive algorithm which is found to be unnecessary and time consuming as well, thus it's being avoided) , let's call them cells whose sizes are determined accurately by two major factors including the corresponding optimum SAR aperture (on the basis of rough priori estimation of mean of spectrum width of a few dominant desired scatterers after ground-clutter filtering. Refer to the results in the previous subsection) and the second is the number of samples which must be enough for accurate estimation in each cell. It's also important to check the SNR at each region to make sure the estimations are reliable.

The corresponding simple topology is visualized in figure (2.10). Here the uniform division is chosen which means that the cell size increases at further ranges.

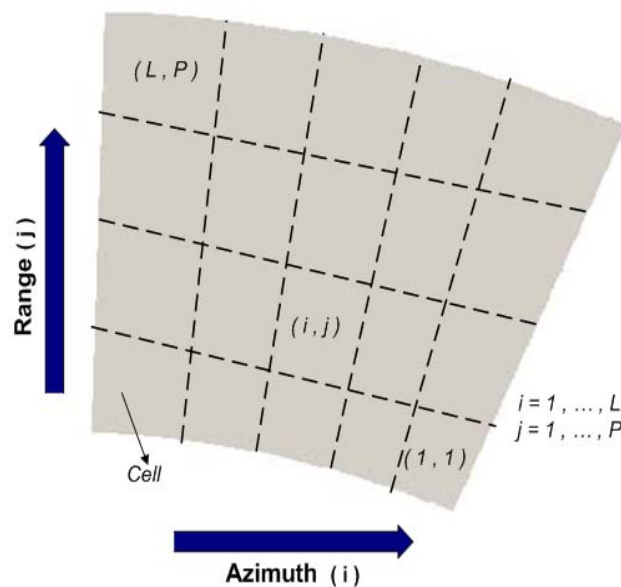


Figure 2.10: Topology of cell division for motion and error compensation

Apart from the linear motion compensation performed along azimuth for each and every single cell, the high order motions ,called phase error which limits the SAR resolution severely in meteorological application of SAR because of several aforementioned reasons (In this case the key condition under which the resolution can be enhanced, depends on the ratio of the phase error's standard deviation and sensor's radial velocity (Atlas and Moore, 1987)) , must be removed to better focus the image or at least prevent it from defocusing such as smearing or blurring effects in processed image introduced

by SAR's post filter as consequence of wide spectrum from highly-disturbed precipitation against narrow-band post filter.

The phase error may also result in phase wrapping (occurs at the presence of uniformly distributed random phase) especially while they are of random type (wide-band phase error) which is the most challenging task in SAR autofocusing compared to its narrow-band counterparts. Particularly, the estimated phase errors from particles of rain with random motion demonstrate wide-band phase error. These random and unknown behaviors of target scene make us to turn to autofocusing algorithm(s) already used for other applications such as ISAR imaging of moving targets based on AUTOCLEAN (Li et al., 2001).

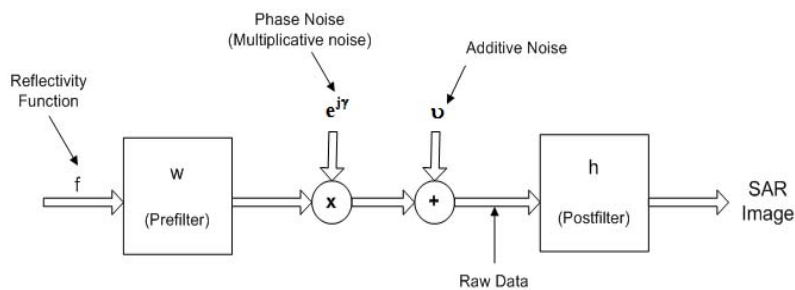


Figure 2.11: The block diagram of the SAR system in phase noise

Here the weighed least-square(WLS) (Ye et al., 1999) method in conjunction with 2-D REALAX (Zheng and Bao, 2000) are employed in the autofocusing approach for precipitation processing. Furthermore; in the AUTOCLEAN algorithm (Zheng and Bao, 2000) it is necessary to compensate for the range misalignment arising from non-linear radial motion which also introduces azimuthal phase error as a result of its non-linear change along cross-range. This mutual effect between azimuthal phase error and range misalignment along with motion estimation make the AUTOCLEAN algorithm iterative particularly for random scene.

Regarding range bin alignment as well as range curvature, the envelope cross-correlation approach (Chen and Andrews, 1980) is taken into account.

The autofocusing method has been used for 2-D SAR compression in both range and azimuth, however; here range migration is not important because no chirp or frequency modulated signal is transmitted in this Doppler weather radar, and thereby it can be disregarded in the preprocessing steps for motion compensation. This especially holds true for small cell compared to the large area of the image.

Since, The SAR image is obtained from the FT of raw data and also the FT

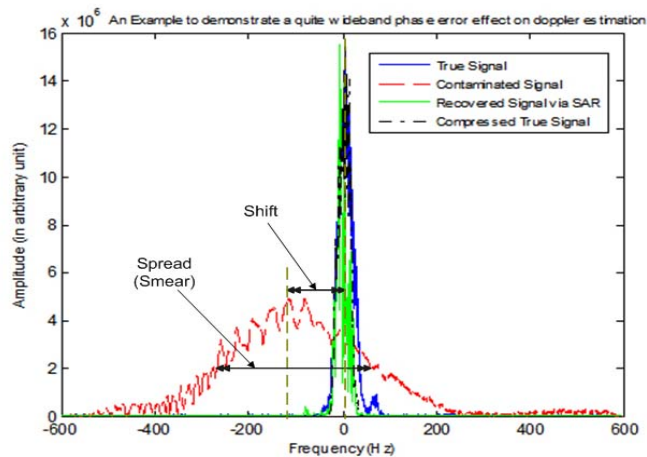


Figure 2.12: An example of narrow-band phase error

is very sensitive to multiplicative noise, phase error, the image is both shifted and smeared after the SAR post filter without phase-error mitigation.

For better understanding, a simple block diagram of a SAR system contaminated by phase error/multiplicative noise and an example regarding effects of this phase noise on a single target as well are shown in figure (2.11) and figure (2.12) respectively. In figure (2.12), phase-noise-free raw samples, processed samples of contaminated data and phase-error-corrected samples are compared together to demonstrate the impacts of the low-order (narrow-band) phase noise with the emphasis on the first and second moments of the FT. As anticipated, the image is shifted and also smeared (the resolution is degraded considerably). You may find a few other examples of the low-order effects of phase noise on true images such as those extracted by DLR-airborne SAR system, in Danklmayer et al. (2005).

Another example regarding the effects of the wide-band (white) phase error on an image is illustrated in figure (2.13). To mitigate the phase error the WLS method (Ye et al., 1999) is used. To get the correct estimation of the wide-band phase error the method takes a quite large number of range bins in which there exist several small scatterers as clutters with a one dominant scatterer as a signal with high enough signal-to-clutter ratio (SCR) which is sorted in descending order and employed as weighting coefficient. In this example the white phase error is inserted artificially. The number of samples in azimuth is high whereas that of useful range bins are small and thereby not enough to fully retrieve the true signal out of its noisy samples. There is still some shift as well as smearing/defocusing at some range bins. Note that none of the results are windowed in order to remove sidelobes in SAR

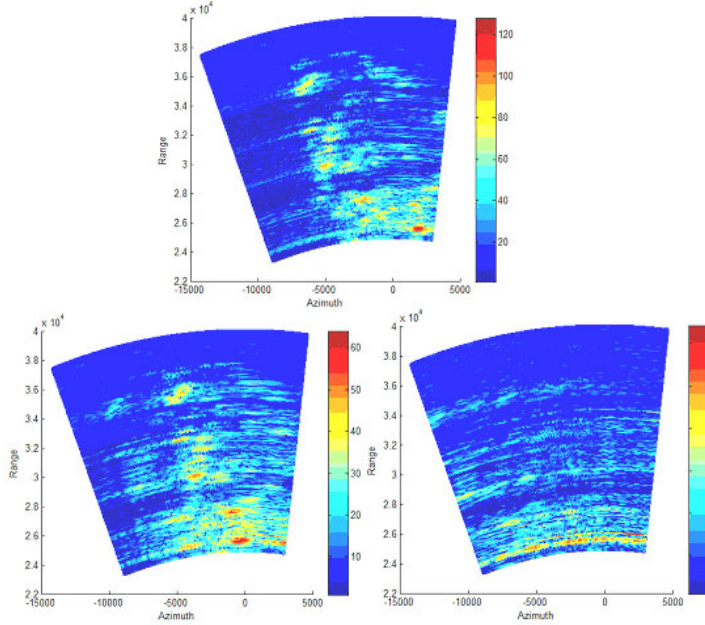


Figure 2.13: An example of wide-band phase error on clutters from Horn,true focused image (top),autofocused by WLS(bottom-left), non-autofocused image(bottom-right)

processor.

One key assumption in WSL is that all range bins used in the algorithm are affected by the same phase error, in other words the phase error is not dependent on the range bin. This fact is totally denied in precipitation imaging as there is another range-dependent phase error due to fluctuation along both range and azimuth. Thus another phase term must be taken into account which is function of both range and azimuth. If one assumes that the phase variation along range is linear (equivalently the wind shear can be assumed to be linear with altitude and the turbulence is not so severe) then the auto-focusing technique proposed by Li et al. (2001) might be used to process the samples.

According to the above-mentioned facts, the new signal model $s_n(m, \bar{m})$ whose error with respect to raw samples must be minimized, is given as

$$s_n(m, \bar{m}) = s(m, \bar{m})e^{r\gamma(m)}e^{j\chi(m)\bar{m}} \quad (2.26)$$

In which the $s(m, \bar{m})$ is defined in equation (2.15).

Herein,the SAR algorithm for precipitation consists of almost the same steps of autofocusing algorithm taken in Li et al. (2001) with 2-D CLEAN model described in previous subsection. As initial values, the phase errors in both range and azimuth are derived from envelope cross-correlation and WLS

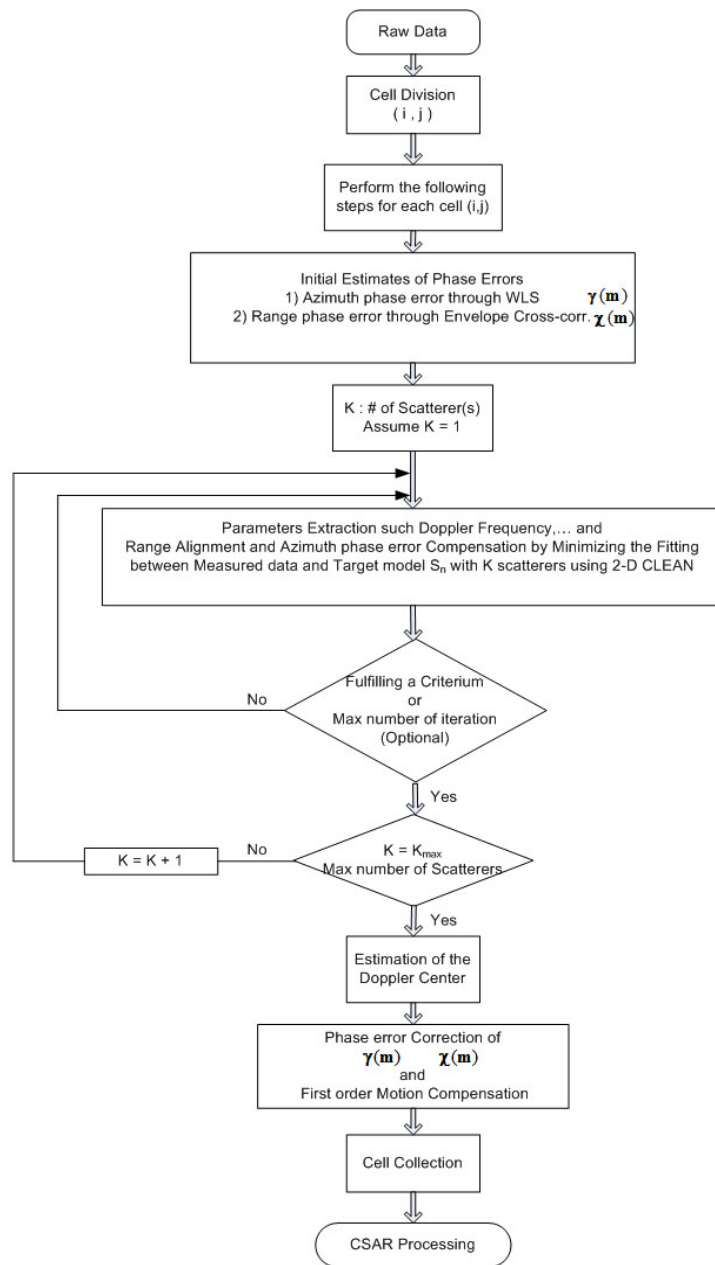


Figure 2.14: Flow Chart of 2-D Autofocus CSAR

method. Again for better motion compensation, the cell-division approach is considered. Figure (2.14) illustrates the flow chart of the corresponding algorithm.

In this analysis, three steps are of key significance illustrated in figure (2.15). Keep in mind that unlike usual SAR systems the range misalignment denotes the azimuth-dependent phase error along range instead of range migration due to SAR system which here is negligible because of both very small phase history and low range resolution in the corresponding CSARs.

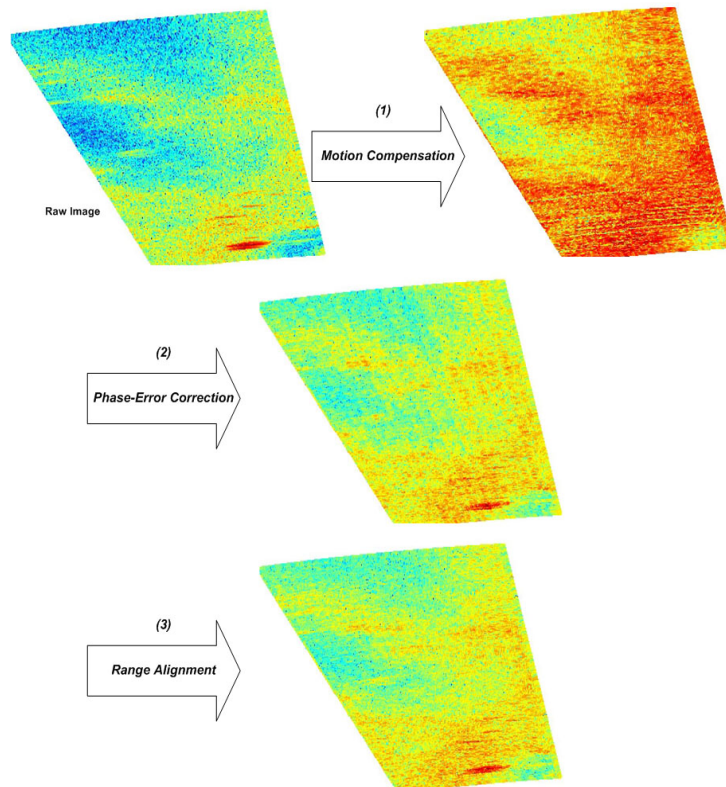


Figure 2.15: Demonstration of the key preprocessing steps in PSAR

The convergence criteria stated in the corresponding paper is not achievable here, as the scene is random (partially coherent) and the number of samples in range for each transmitted pulse is not enough to force the phase-error estimations to become stable. It is true to say that the assumed model is not accurate enough due to random and nonlinear behavior of the scene with distributed targets. However by limiting the region under process like cell division explained above, the variance of the error decreases considerably and the results get better. By doing so, the iterative process in the flow chart of figure(2.14) may be avoided to speed up the process. Note that for the esti-

mation of phase errors, 2-D CLEAN approach based on point scatterers rather than distributed model is good enough. To make a more reliable estimation one may use RELAX instead of CLEAN at the expense of computational burden.

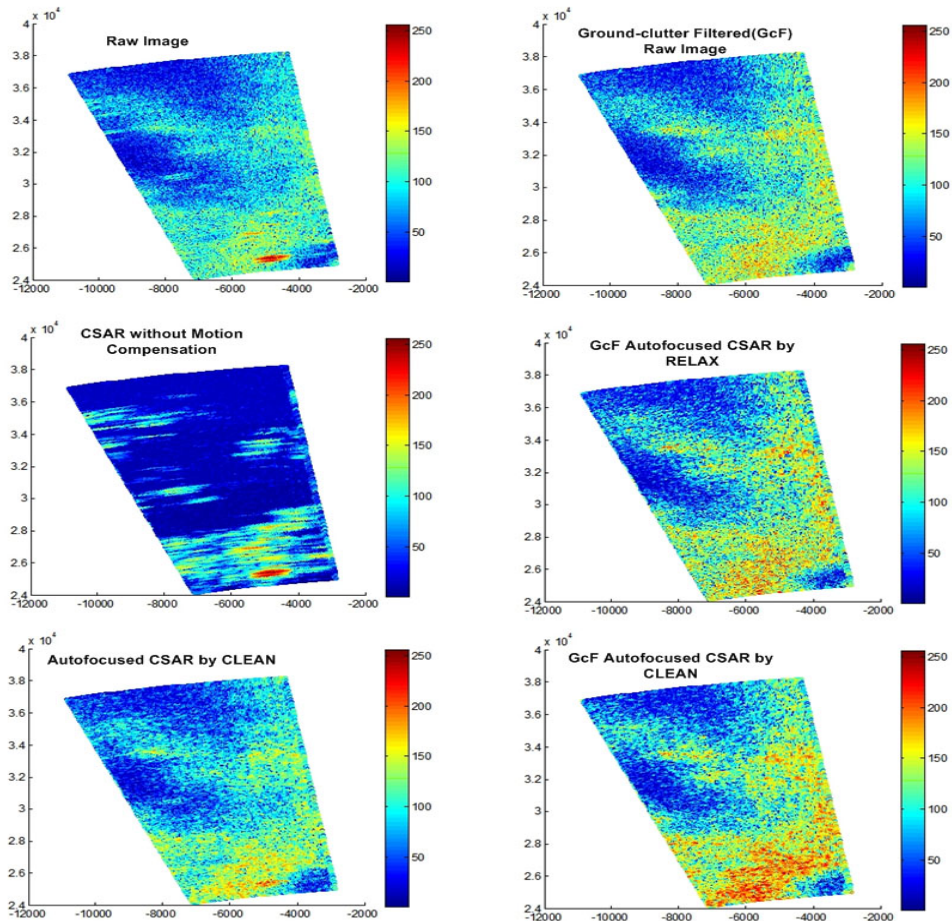


Figure 2.16: Raw and focused images of the reflector in rain

Figure (2.16) illustrates the raw image, ground-clutter filtered image and their corresponding focused and autofocused images with CLEAN and RELAX methods from data of reflector antenna in rain. As anticipated the resolution won't improve neither for precipitation nor for clutters. Here due to the small number of samples the cell division is not performed.

According to the figure(2.16) when the image is simply focused without any motion compensation, only the ground clutters if quite stationary, remain focused and the rest of the target areas in the image, depending on its velocity and variance of the phase error, (high order motions which cause spread

in Doppler domain) becomes defocused i.e., smeared and shifted from their true positions. While trying to focus the precipitation area the ground clutterers get defocused and thereby their amplitude don't increase by coherent processing. As a consequence the desired area manifest itself more clearly and dominantly compared to the raw image in the presence of strong clutterers showing up in the image due to perhaps either strong sidelobe(s) or propagation anomalies of the atmosphere which have caused refraction in radiated electromagnetic waves not supposed to hit the ground within specific ranges.

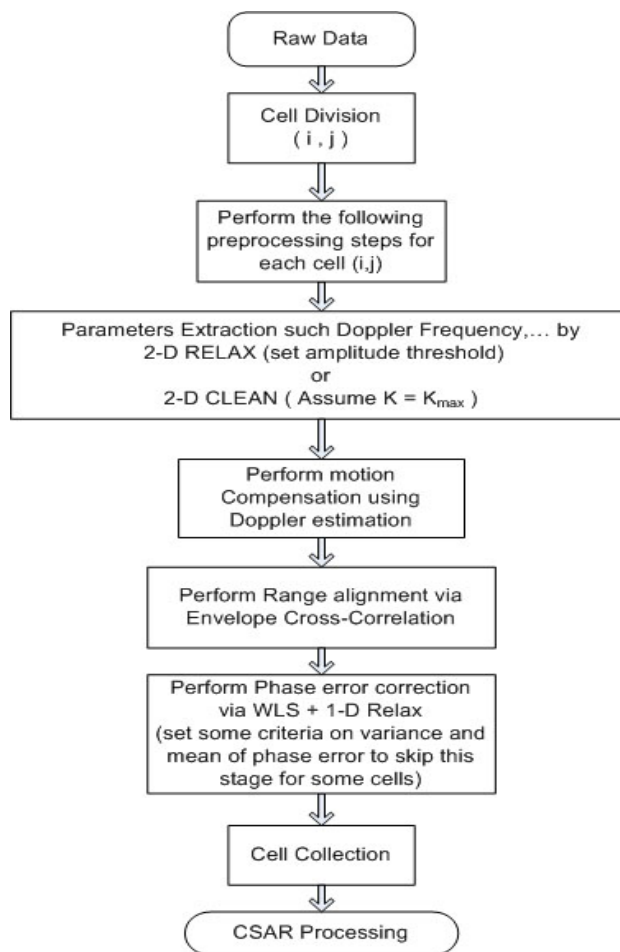


Figure 2.17: Flow Chart of a faster 2-D Autofocus CSAR

In the autofocusing algorithm, one can set both statistical-based threshold for phase error (e.g., set a mean and variance threshold for phase correction along azimuth) as well as amplitude threshold for motion estimation to circumvent unnecessary compensation for some cells with very low SNR or

even avoid parameter estimation of those very weak scatterers to accelerate the process. Thus those patches (cell regions) that appear uniform with single color i.e.,single low intensity, are avoid of any target and simply exhibit amplified noise as a result of constructive summation. Consequently an alternative algorithm which is non-iterative and thereby faster than its previous counterpart, is presented in figure (2.17).

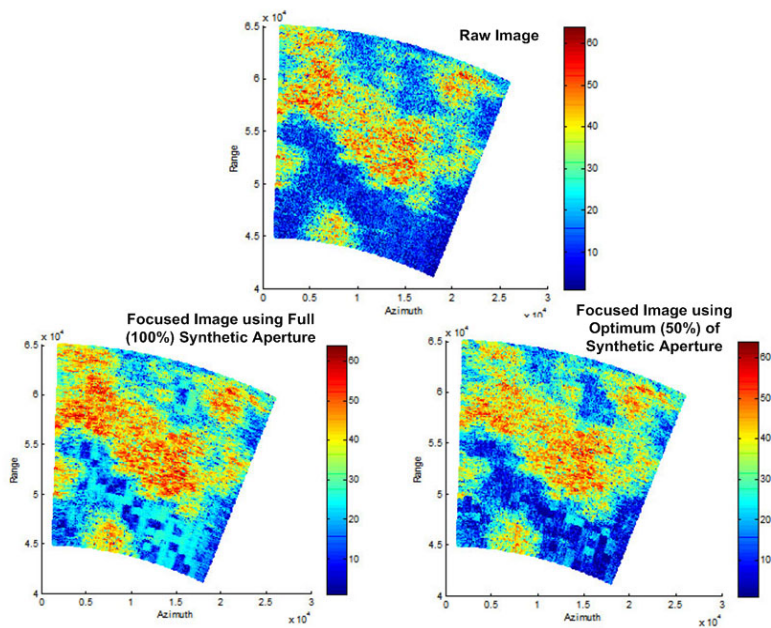


Figure 2.18: Raw and processed images from reflector in rain

The following couple of examples have gained its results through this algorithm.

Figure(2.18) shows raw and focused images from the reflector in moderate rain. Those above-mentioned patches are noticeable for the full synthetic aperture whose integration time is about 34 ms. On the other hand for half of the full aperture this effect is mitigated. To find out the optimum aperture one may plot the increase in dynamic range(DR) versus the number of samples within synthetic aperture corresponding to the various sizes (i.e., at several integration time) and pick the point after which the curve begins to bend or saturate as depicted in figure(2.19).

As expected the optimum aperture occurs at integration time or decorrelation time T_d , i.e. the interval when the coherent integration is maintained,proportional to the inverse of Doppler spectral width (here the median value of Δ_a can be considered due to its Rayleigh-like distribution,however; since this might happen due to high spread values at very low SNR areas

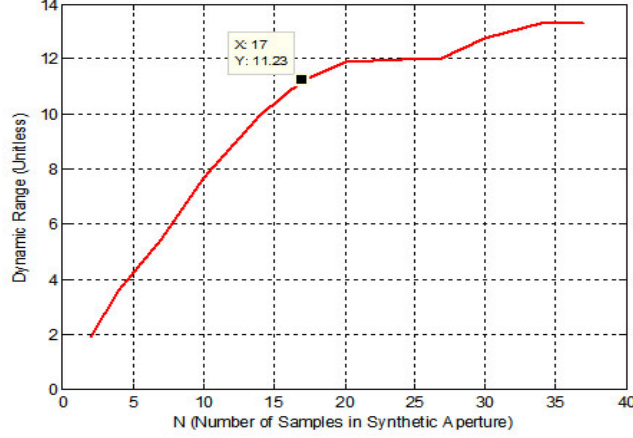


Figure 2.19: DR versus N for the reflector

for the reflector, we may ignore those values and therefore the distribution resembles Gaussian shape like that of horn, in this case the mean value can be taken which is quite the same for both antennas), which is given (Atlas and Moore, 1987)

$$T_d = \frac{1}{\Delta_a} \quad (2.27)$$

Applying the median value and mean already estimated to the equation (2.27), the decorrelation time becomes about 18 ms and 14 ms respectively, which is close to that estimated optimum value marked in figure(2.19) (in this figure, the marked number of samples must be multiplied by PRI to be converted into time unit) for the reflector experiment.

The processed gain as a function of synthetic aperture samples is drawn in figure (2.20) based on both theory (Metcalf and Holm, 1979) and experimental result. These curves are very similar for the standard deviation of Doppler velocity, σ_v around 0.9 m/s (in fact this is close to the mean value of Doppler spread of reflector which proves that the very low-probable high values of Doppler spread for reflector might be improper. Thus the assumed Gaussian distribution in the corresponding reference matches with experimental results) based on Gaussian distribution of Doppler velocity.

According to figure(2.20), the Gain is approximately quadratic in N for small value of N but becomes nearly linear as N becomes larger and finally beyond a certain value of N, its quadratic behavior is lost and the power gain increases in a manner corresponding to incoherent integration of samples similar to that of decorrelated samples of noise.

For the horn antenna, as the estimated probability density function deviates

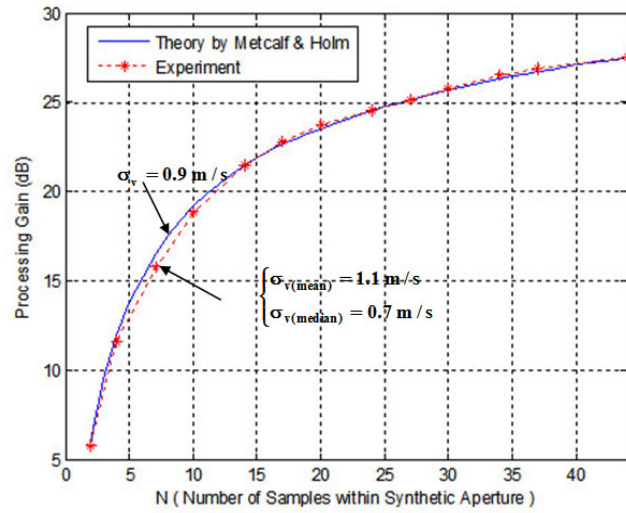


Figure 2.20: Processing Gain versus N for the reflector and the theory

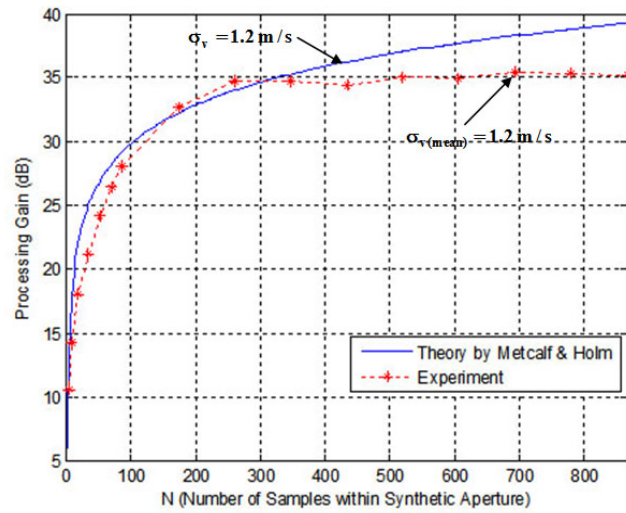


Figure 2.21: Processing Gain versus N for the horn and the theory

to some degree from that of Gaussian, the corresponding results by theory and experiment would be a little bit different. The power gains of those are plotted in figure(2.21) for $\sigma_v = 1.2$ m/s.

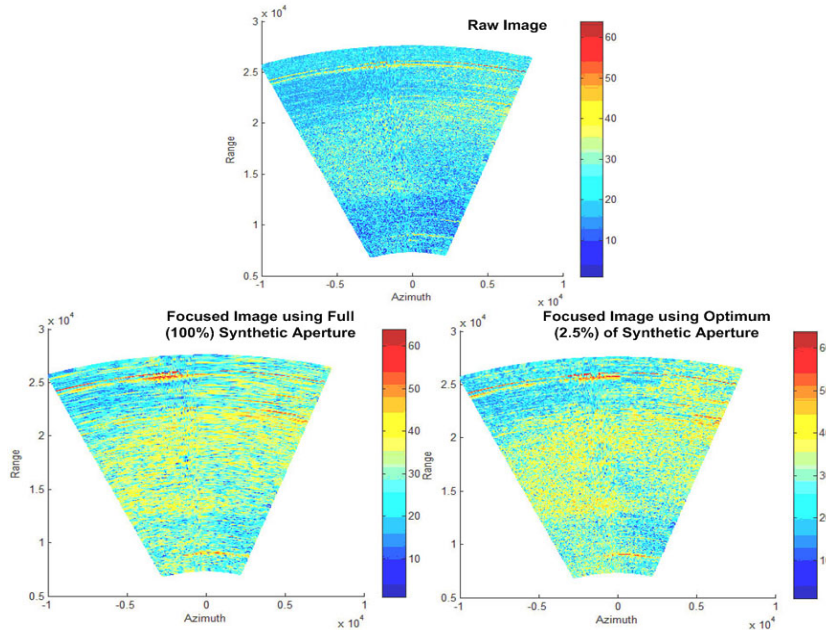


Figure 2.22: Raw and processed images from horn in rain

Similar to the reflector, the raw image and focused images using full and optimum synthetic aperture, of horn are plotted in figure(2.22). Since the resolution is dominantly constrained by target rather than the SAR system, here again the optimum decorrelation time is about 18 ms related to about 0.025 times of maximum achievable integration time which is about 700 ms for the horn system. Thus the resolution doesn't improve even for high-capable SAR system such as that of horn which gives very high azimuth resolution for coherent scene such those of ground clutters. Nevertheless, the only change occurs in SNR increasing by the processing gain. The amount of increase is less than that of expected value for coherent scene/narrow width spectrum. The amount of gain reduction for optimum aperture is about 7.7 dB which is very close to the theoretical value, 8 dB obtained by Metcalf and Holm (1979) for the same Doppler spread and almost the same radar parameters. Unlike the coherent scene/ fixed surface targets the angular resolution (or equivalent synthetic beamwidth) for random/partially coherent scene containing distributed targets such as meteorological ones, is manipulated by the two key parameters, platform velocity and Doppler spectral width (or variance of Doppler velocity), irrespective of the antenna's beamwidth in the following

way (Atlas and Moore, 1987)

$$\theta_s = a \frac{\sigma_v}{V_r} \quad (2.28)$$

in which factor “ a ” has the value between 2 and 2.35 (asymptotic value for large variance of Doppler velocity). It is of key significance to note that the achieved resolution has nothing to do with the size or beam resolution of the antenna. This has been already apparent from the processing gain plots for two different antenna in figures (2.20) and (2.21). Moreover; the larger the distance D the better the resolution since the radial velocity in CSAR doesn’t only depend on angular velocity but also the radius of circle. The achieved synthetic angular resolution for horn is about 54.7° approximately half of that of reflector. However; the resultant angular resolution, θ_r , for horn and reflector are about 23.6° and 1° respectively, according to Atlas and Moore (1987) as

$$\theta_r = \frac{\theta_s \theta_H}{\sqrt{\theta_s^2 + \theta_H^2}} \quad (2.29)$$

Despite the final/resultant angular resolution of both cases, the resolution is simply enhanced a little bit for horn, about 2° in theory, compared to its real beamwidth.

In order to improve the resolution by ground-based circular PSAR such as horn, the maximum Doppler spread in the imaging scene must be

$$\sigma_{v_{max}} \approx \frac{\pi}{180} rpm \theta_H D \quad (2.30)$$

For the horn case the maximum allowable spectral width is about 0.19 m/s which is very small for many meteorological phenomena. To understand how small the maximum Doppler spread is for the ground-based SAR system in contrast with that of airborne-based and spaceborne-based SAR systems (Atlas and Moore, 1987), a simple comparison is made for these three systems in table(2.1).

Table 2.1: Max. Doppler Spectral Width σ_v for which $\theta_r \approx \theta_s$

Platform Type	λ (cm)	l_h (m)	V_r (m/s)	σ_v (m/s)
Ground-based CSAR	5.4	0.122	2.5	0.19
Airborne-based SAR	5.7	1.5	150	0.88
Spaceborne-based SAR	5.7	12	7000	5.5

As implementation of both large D and high rpm is almost impossible for

ground-based CSAR, the only alternatives are air-borne based SAR (Atlas et al., 1977; Atlas and Moore, 1987) and space-borne based SAR (Atlas and Moore, 1987; Moore et al., 1996; Moore and Ahamad, 1993; Martinez and Alvarez-Perez, 2006) in order to obtain high resolution to a limited degree for meteorological application.

2.2 Reflectivity and Rain Rate Estimation

The conventional radar equation for distributed targets particularly precipitation is (Doviak et al., 1979)

$$P_{av} = C_r \times \frac{l_{rain}^2 \eta}{R_n^2} \quad (2.31)$$

where

$$C_r = \frac{P_t G_a^2 \lambda^2 L_r c \tau \theta_H \theta_V}{1024 \pi^2 \ln 2} \quad (2.32)$$

$$l_{rain} = 10^{-3} K_r \times R_n \quad (2.33)$$

$$\eta = 0.93 \frac{\pi^5}{\lambda^4} Z \quad (2.34)$$

Attenuation or absorption factor, K_r , in rain depends on the rain rate and the wavelength as well. A rough closed-form expression obtained via curve fitting at C-band (estimated by the author) is given as

$$K_r \approx 0.003 R_r^{1.22} \quad (2.35)$$

Before the estimation of reflectivity factor, the averaging is performed on power samples (derived from I and Q samples of raw data) and then the available averaged noise power is subtracted from it to calculate the averaged power of the received signal void of noise, P_{av} .

Note that the equation (2.31) is used for distributed scatterers or volume scatterers. Regarding clutters such as those of ground, birds, airplane (man-made targets) and in general surface scatterer the radar equation would be somehow different, because there are surface scatterers in return. However; since the scene consists of amalgam of both desired targets and clutters and also for the sake of comparison between these two in order to identify and distinguish clutters from signals, the same radar equation is going to be used for all of them. In other words the reflectivity factors of all kinds of targets are put in dBZ which is

$$dBZ = 10 \log_{10} Z$$

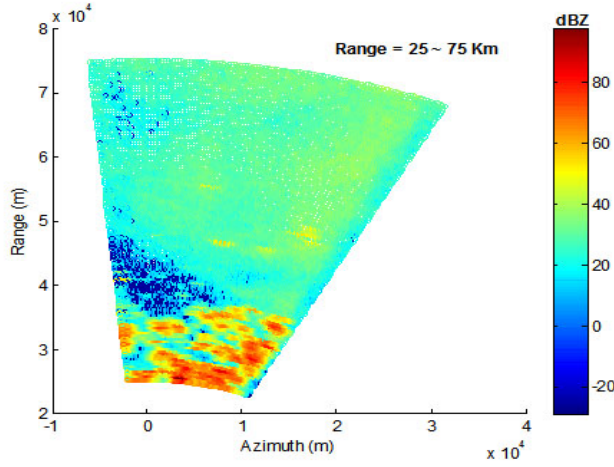


Figure 2.23: The reflectivity pattern of rain by reflector on raw data

The rain rate is associated with reflectivity factor approximately in the following manner

$$Z = 200R_r^{1.6} \quad (2.36)$$

Alternatively for the stratiform rain in which the reflectivity factor is almost uniform and less than 40 dBZ, or widespread weak showers in which the reflectivity factor is less than 45 dBZ (these two are the precipitation condition for the examples brought up in this section) one may employ the following equation instead (Fang and Doviak, 2001),

$$Z = 23 + 16 \log_{10} R_r \quad (2.37)$$

Unlike the previous equation, in this equation Z must be in dBZ.

As an example the reflectivity pattern of rain taken by reflector at far ranges is illustrated in figure(2.23). The range and cross range resolution after the power averaging of the raw data are 400 m and 1° respectively. Those regions with reflectivity ranging from 20 dB up to 45 dB are precipitation areas which denote stratiform rain or weak showers. The probability distribution of the corresponding rain rate of these areas are depicted in figure(2.24). The mean value of the rain rate is about 3 mm/hr which denotes the weak sporadic shower which was simply observable within that azimuthal interval.

On the other hand, according to figure(2.25) and (2.26) of reflectivity factor and rain rate's probability distribution of data obtained from horn at the lower ranges respectively, the rain rate seems higher and cover almost a large azimuthal interval. The corresponding mean value of the rain rate at such

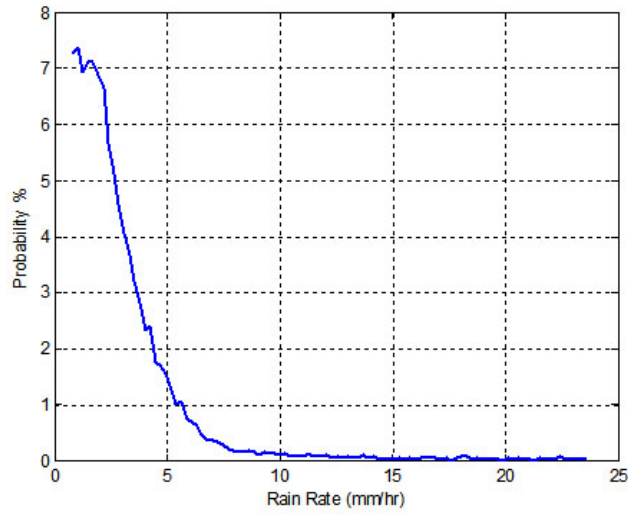


Figure 2.24: The probability of rain rate obtained from reflector

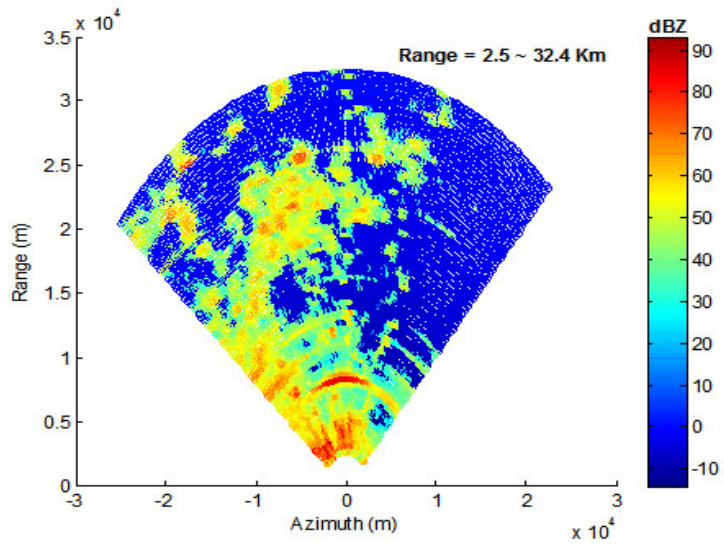


Figure 2.25: The reflectivity pattern of rain by horn on raw data

low distances for such stratiform moderate shower is about 10.5 mm/hr.

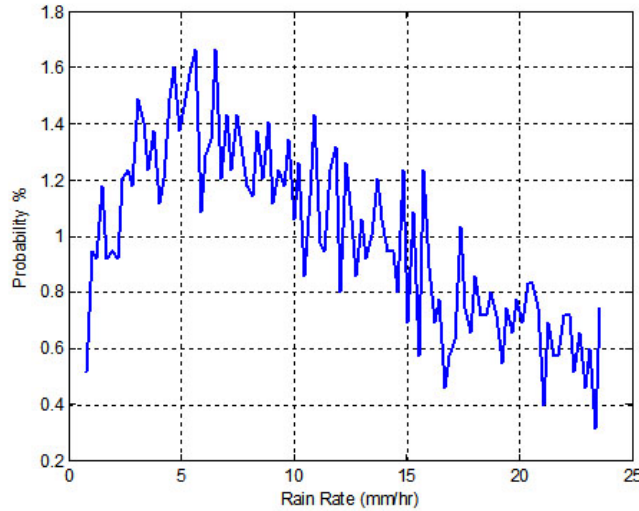


Figure 2.26: The probability of rain rate obtained from horn

For the PSAR, θ_H must be replaced by the resultant pattern obtained from equation(2.29). Besides, another factor attributed to the processing gain of SAR must be included in the radar equation of PSAR. This factor depends on three parameters, wavelength, PRF and Doppler spectral width σ_v .

Following the approach of Atlas and Moore (1987) in almost similar way, the final equation of processed power (at the output of the post filter), P_{psar} , as a function of averaged power of the conventional Doppler weather radar, P_{av} , is

$$P_{psar} = \frac{\lambda\theta_r PRF}{4\theta_H\sigma_v} \times P_{av} \quad (2.38)$$

From equation (2.38) it can be easily deduced that the narrower the spectrum width the stronger the processed signal due to the larger coherency of samples under integration. As $\theta_r \approx \theta_H$ for precipitation in ground-based PSAR, these two may be removed from the above equation without causing any serious error. Thus the only critical and variable parameter left in determination of reflectivity factor of precipitation from the processed data is the Doppler spectral width which is in opposite to that of spaceborne-based PSAR (Atlas and Moore, 1987). Nevertheless; this multiplicative factor is almost negligible for precipitation. On the contrary it has quite high value for ground clutters particularly those stationary ones which are very strong. This fact can be taken as a benefit in separating the clutters from precipitation in both reflectivity and rain rate estimation and thereby mitigating the

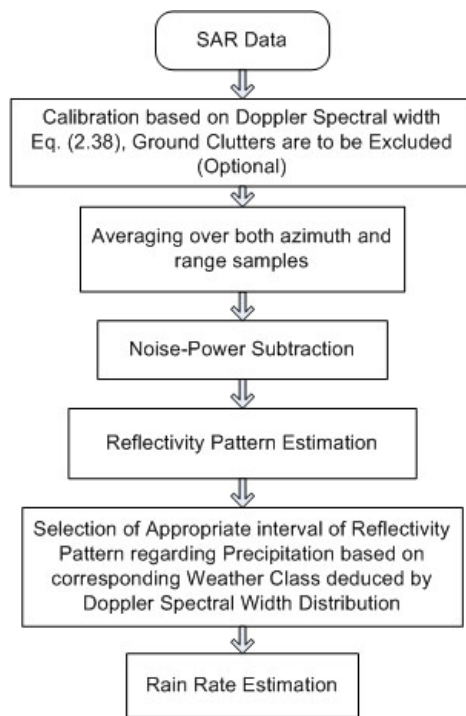


Figure 2.27: The flow chart of rain rate estimation

regarding bias caused by ground clutters. The flow chart used to perform the rain rate estimation from the SAR data is brought in figure(2.27).

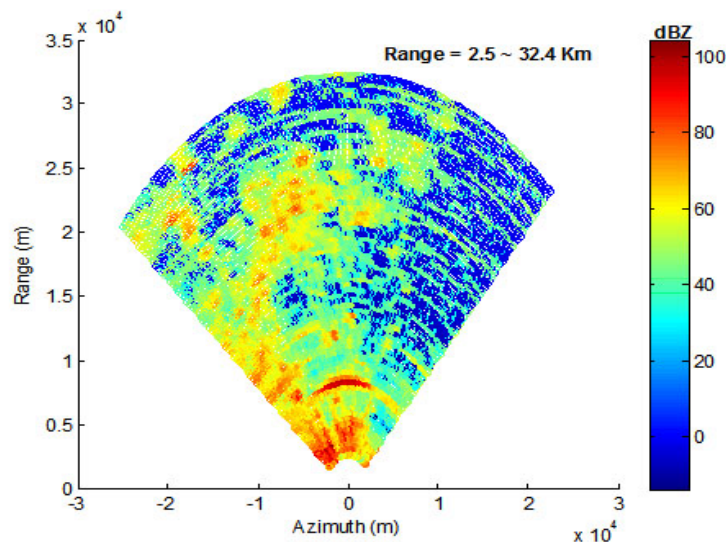


Figure 2.28: The reflectivity pattern from horn of non-filtered processed data

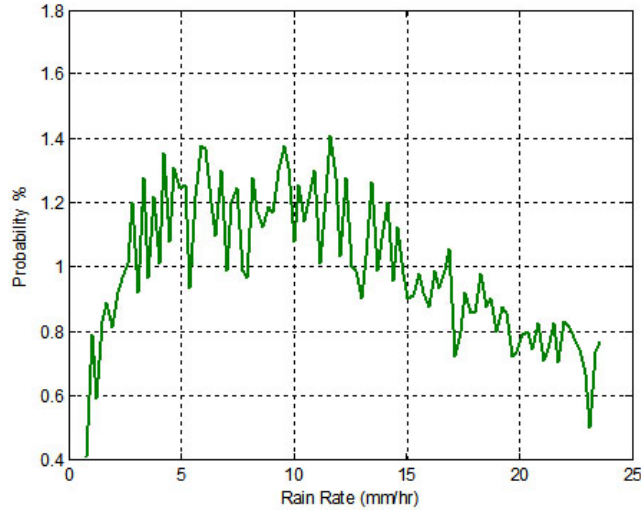


Figure 2.29: The probability of rain rate obtained from horn after processing

Figure (2.28) and (2.29) show the reflectivity factors and their corresponding rain rate's probability distribution estimated by the above-mentioned approach, respectively. The median rain rate is about 11 mm/hr which denotes a moderate and stratiform rain at near ranges.

It is evident that the results regarding rain rate distribution estimated from horn's data have quite high fluctuation. The reason is that the horn's antenna beamwidths especially the vertical beamwidth is very wide, about 23° in contrast to that of reflector whose beamwidth is about 1° . This means that the volume for which the both reflectivity and rain rate are calculated, is much bigger for horn antenna and that leads to more bias and errors not only in estimation of precipitation parameters but also in Doppler spectral width estimation illustrated in the previous subsection. Moreover; according to various weather phenomena (by weather phenomena here it means various rain class) as well as the Doppler spectral width distribution of which cumulative probability (that has quite low median value due to bias imposed by strong remained clutters with narrow spectrum width) plotted in figure (2.30), the rain rate is estimated from reflectivity between 20 and 45 dBZ in order to remove irrelevant reflectivities from non-precipitation targets. Those high reflectivities are associated with clutters since the rain is stratiform or weak spread shower.

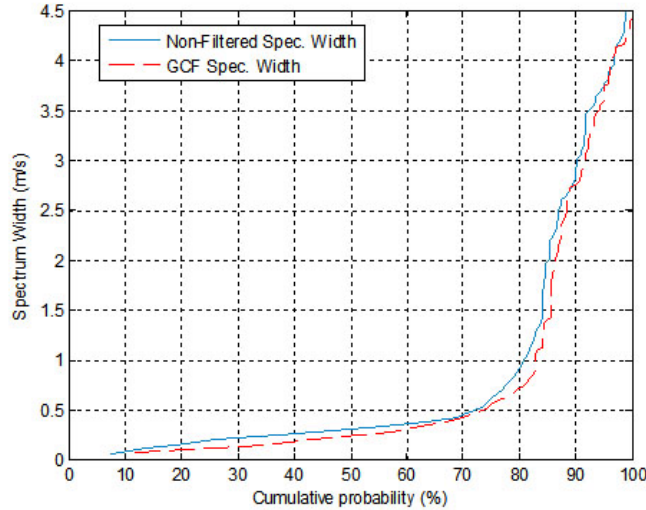


Figure 2.30: The cumulative probability of σ_v of both ground-clutter filtered(GCF) and non-filtered data obtained from horn after processing

2.3 Concluding Remarks

Because of the random motion of the precipitation which makes the samples incoherent as well as the low velocity of the ground-based platform (relative to the speed of the velocity change of the target scene) the ground-based PSAR can hardly fulfill the SAR's resolution capability achieved in fixed and coherent surface or man-made targets. In other words for both systems, i.e. reflector and horn, irrespective of their antennas' sizes, their velocity-to-Doppler-velocity-width ratio is not big enough to create coherent samples of the desired scene. Bear in mind that the reflector is not even capable to improve resolution for a stationary point target, exemplified in chapter one, due to its big size along azimuth i.e., very narrow beamwidth, compared to its radius of rotation D (platform size).

Another limitation for rain rate measurement is the surface clutters which can bias severely the reflectivity and rain estimate. Moreover, if not filtered out, they may also bias the spectrum width estimates. This latter effect, however; can be mitigated in CLEAN or RELAX algorithms by setting a condition before averaging of the whole estimates within each and every single cell. By doing so, the necessity of filtering ground-clutter coming from either main beam or sidelobes might be avoided.

Another significant factor in reliable estimation of meteorological parameters is the cross-track or vertical size of antenna which defines the resolution volume covering scatterers at different height. The bigger the corresponding

beamwidth, the poorer and less reliable the estimation of rain reflectivity and rain rate. Besides it has a serious impact on the Doppler parameter estimation such as Doppler velocity and Doppler spectral width. This is unfortunately the dominant ill-effect in horn case. Its vertical beamwidth is very big which makes estimates suspicious.

As a consequence the desired system for ground-based circular PSAR would be the one which includes antenna with quite small along-track size (almost large horizontal beamwidth) and large cross-track size (narrow vertical beamwidth) rotating at fast velocity as possible on a quite big platform (large D compared to antenna's along-track size such as that of horn employed here). However; as stated before, the key limitation of the desired system, in terms of resolution, would be the realization of the high-speed rotating ground-based platform in order to enhance azimuthal resolution even under non-stormy and mild rain circumstances let go of the severe weather conditions such as severe convective storms or rain/snow squalls.

In short, one can conclude that a ground-based stripmap SAR system supposed to be used in imaging of random scene (very short coherent scene such as weather targets) is almost devoid of SAR's capabilities in improvement of azimuthal resolution.

Bibliography

- D. Atlas and R. K. Moore. The measurement of precipitation with synthetic aperture radar. *J. of Atmospheric and Oceanic Tech.*, Vol. 4:pp. 368–376, September 1987.
- D. Atlas, C. Elachi, and W. E. Brown. Precipitation mapping with an airborne synthetic aperture imaging radar. *Journal of Geophysical Research*, VOL. 82:pp. 3445–3451, August 1977.
- C. A. Balanis. *Antenna theory: analysis and design*. Hoboken, N.J, Wiley, 2005.
- Z. Banjanin, D. S. Zrnic, and J. R. Cruz. A linear prediction approach to doppler mean frequency retrieval in the presence of ground clutter. *IEEE Trans. Aerosp. Electron. Syst.*, Vol. 29:pp. 1050–1058, July 1993.
- Z. Bi, J. Li, and Z. Liu. Super resolution sar imaging via parametric spectral estimation method. *IEEE Trans. Aerospace and Electronic Systems*, Vol. 35:pp. 267–281, January 1999.
- A. Broquetas, R. DePorreta, L. Sagues, X. Fabregas, and L. Jofre. Circular synthetic aperture radar (c-sar) system for ground-based applications. *ELECTRONIC LETTERS*, Vol. 33(11):pp. 988–989, May 1997.
- W. M. Brown. Synthetic aperture radar. *IEEE Trans. Aerosp. Electron. Syst.*, vol.AES-3:pp. 217–229, Mar. 1967.
- W. M. Brown. Sar resolution at the presence of phase error. *IEEE Trans. Aerosp. Electron. Syst.*, Vol. 24:pp.808–814, November 1988.
- W. M. Brown and J. F. Riordan. Resolution limits with propagation phase errors. *IEEE Trans. on Aerosp. Electron. Syst.*, AES-6:pp. 657–662, September 1970.

- H. L. Chan and T. S. T. S. Yeo. Comments on “non-iterative quality phase gradient autofocus (qpga) algorithm for spotlight sar imagery. *IEEE Trans. Geoscience and Remote Sensing*, Vol. 40:pp. 2517, November 2002.
- H. L. Chan and T. S. Yeo. Noniterative quality phase-gradient autofocus (qpga) algorithm for spotlight sar imagery. *IEEE Trans. Geoscience and Remote sensing*, Vol. 36:pp. 1531–1538, September 1998.
- C. Chen and H. C. Andrews. Target-motion-induced radar imaging. *IEEE Trans. Aerospace and Electronic Systems*, Vol. AES-16:pp. 2–14, January 1980.
- W. Chen, G. Zhou, and G. B. Giannakis. Velocity and acceleration estimation of doppler weather radar/lidar signals in colored noise. *IEEE Proc.*, Vol.: pp. 2052–2055, 1995.
- A. Danklmayer, K. A. C. de Macedo, R. Sceiber, T. Boerner, and M. Chandra. Analysis method of errors (motion and atmospheric) in synthetic aperture radar (sar) images. *Advances in Radio Science*, Vol. 3:pp. 1–4, 2005.
- R. J. Doviak, D. S. Zernic, and D. S. Sirmans. Doppler weather radar. *IEEE Proc.*, Vol. 67:pp. 1522–1556, November 1979.
- M. Fang and R. J. Doviak. Spectrum width statistics of various weather phenomena. Technical report, National Severe Storms Laboratory, 2001.
- G. Franceschetti and R. Lanari. *Synthetic Aperture Radar Processing*. Boca Raton, CRC Press, 1999.
- C. Greene and R.T.Moller. The effect of normally distributed random phase errors on synthetic array gain patterns. *IRE Trans. Mil. Electron*, MIL-6: pp. 130–139, April 1962.
- L. H. Janssen and G. A. Vanderspek. The shape of doppler spectra from precipitation. *IEEE Trans. Aerospace and Electronic Systems*, Vol. AES-21:pp. 208–219, March 1985.
- S. M. Kay. Noise compensation for autoregressive spectral estimates. *IEEE Trans. Acoustics, Speech, and Signal Processing*, Vol. ASSP-28:pp. 292–303, June 1980.
- S. M. Kay and S. L. Marple. Spectrum analysis—a modern perspective. *IEEE Proc.*, Vol. 69:pp. 1380–1419, November 1981.

- J. Lee. Poly-pulse estimation in a doppler weather radar. *IEEE Proc.*, Vol.: pp. 1968–1970, 2000.
- J. Li and P. Stoica. Efficient mixed-spectrum estimation with application to target feature extraction. *IEEE Trans. Signal Processing*, Vol. 44:pp. 281–295, February 1996.
- J. Li, R. Wu, and V. C. Chen. Robust autofocus algorithm for isar imaging of moving targets. *IEEE Trans. Aerospace and Electronic Systems*, Vol. 37: pp. 1056–1068, July 2001.
- Z. S. Liu and J. Li. Feature extraction of sar targets consisting of trihedral and dihedral corner reflectors. *IEE Proc. Radar, Sonar Navig.*, Vol. 145: pp. 161–172, June 1998.
- P. R. Mahapatra and D. S. Zrnic. Practical algorithms for mean velocity estimation in pulse doppler weather radars using a small number of samples. *IEEE Trans. Geoscience and Remote sensing*, Vol. GE-21:pp. 491–501, October 1983.
- R. J. Mailloux. *Phased- array antenna handbook*. Artech House, 2ed Edition, 2005.
- J. M. Martinez and J. L. Alvarez-Perez. A first study on the use of terrasars-x for meteorological purposes. *IEEE Proc.*, Vol:pp. 1–4, 2006.
- J. I. Metcalf and W. Holm. Meteorological applications of synthetic aperture radar. Technical report, Final Rep. Proj. A-2101, Eng. Experiment Station, Georgia Inst. of Technology, 1979.
- R. K. Moore and A. Ahamad. Limitation on the use of spaceborne imaging sar as rain radars. *Proc. IGARSS*, Vol.:pp. 1021–1024, 1993.
- R. K. Moore, A. Mogili, Y. Fang, B. Beh, and A. Ahamad. Rain measurement with sir-c/x-sar. *Proc. IGARSS*, Vol. 96-3:pp. 1–4, 1996.
- R. K. Raney. Sar response to partially coherent phenomena. *IEEE Trans. on Antennas and Propagation*, VOL. AP-28:pp.777–787, November 1980.
- J. Tsao and B. D. Steinberg. Reduction of sidelobe and speckle artifacts in microwave imaging : the clean technique. *IEEE Trans. on Antennas and Propagation*, Vol. 4:pp. 543–556, April 1988.

- D. E. Wahl, P. H. Eichel, D. C. Ghiglia, and C. V. J. JR. Phase gradient autofocus—a robust tool for high resolution sar phase correction. *IEEE Trans. AES*, Vol. 30:pp. 827–835, July 1994a.
- D. E. Wahl, C. V. J. Jr., P. A. Thompson, and D. C. Ghiglia. New approach to strip-map sar autofocus. In *Proc. IEEE 6th Digital Signal Processing Workshop*, 1994b.
- W. Ye, T. S. Yeo, and Z. Bao. Weighted least-squares estimation of phase errors for sar/isar autofocus. *IEEE Trans. Geoscience and remote sensing*, Vol. 37:pp. 2487–2493, September 1999.
- Y. Zheng and Z. Bao. Autofocusing of sar images based on relax. *IEEE International Radar Conference*, Vol.:pp. 533–538, 2000.